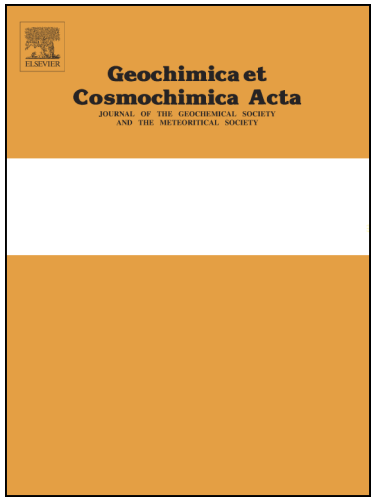

A 1.5 Ma record of plume-ridge interaction at the Western Galápagos Spreading Center (91°40'-92°00'W)

Antje Herbrich, Folkmar Hauff, Kaj Hoernle, Reinhard Werner, Dieter Garbe-Schönberg, Scott White

PII: S0016-7037(16)30205-8
DOI: http://dx.doi.org/10.1016/j.gca.2016.04.036
Reference: GCA 9731

To appear in: *Geochimica et Cosmochimica Acta*

Received Date: 28 July 2015
Accepted Date: 19 April 2016

Please cite this article as: Herbrich, A., Hauff, F., Hoernle, K., Werner, R., Garbe-Schönberg, D., White, S., A 1.5 Ma record of plume-ridge interaction at the Western Galápagos Spreading Center (91°40'-92°00'W), *Geochimica et Cosmochimica Acta* (2016), doi: http://dx.doi.org/10.1016/j.gca.2016.04.036

A 1.5 Ma record of plume-ridge interaction at the Western Galápagos Spreading Center (91°40'-92°00'W)

Antje Herbrich[1*$], Folkmar Hauff[1], Kaj Hoernle[1, 2], Reinhard Werner[1], Dieter Garbe-Schönberg[2], Scott White[3]

[1] GEOMAR Helmholtz Centre for Ocean Research Kiel, Wischhofstraße 1-3, D-24148 Kiel, Germany

[2] Institute of Geosciences, University of Kiel, Ludewig-Meyn-Strasse 10, D-24118 Kiel, Germany

[3] Department of Earth and Ocean Sciences, University of South Carolina, Columbia, South Carolina, USA

* corresponding author

[$] now at State Authority for Mining, Energy and Geology, Hannover, Germany

Abstract

Shallow (elevated) portions of mid-ocean ridges with enriched geochemical compositions near hotspots document the interaction of hot geochemically enriched plume mantle with shallow depleted upper mantle. Whereas the spatial variations in geochemical composition of ocean crust along the ridge axis in areas where plume-ridge interaction is taking place have been studied globally, only restricted information exists concerning temporal variations in geochemistry of ocean crust formed through plume-ridge interaction. Here we present a detailed geochemical study of 0-1.5 Ma ocean crust sampled from the Western Galápagos Spreading Center (WGSC) axis to 50 km north of the axis, an area that is presently experiencing a high influx of mantle material from the Galápagos Hotspot. The

tholeiitic to basaltic andesitic fresh glass and few bulk rock samples have incompatible element abundances and Sr-Nd-Pb isotopic compositions intermediate between depleted normal mid-ocean-ridge basalt (N-MORB) from >95.5°W along the WGSC and enriched lavas from the Galápagos Archipelago, displaying enriched (E-)MORB type compositions. Only limited and no systematic geochemical variations are observed with distance from the ridge axis for <1.0 Ma old WGSC crust, whereas 1.0-1.5 Ma old crust trends to more enriched isotopic compositions in $^{87}Sr/^{86}Sr$, $^{143}Nd/^{144}Nd$, $^{207}Pb/^{204}Pb$ and $^{208}Pb/^{204}Pb$ isotope ratios. On isotope correlation diagrams, the data set displays correlations between depleted MORB and two enriched components. Neither the geographically referenced geochemical domains of the Galápagos Archipelago nor the end members used for principle component analysis can successfully describe the observed mixing relations. Notably an off-axis volcanic cone at site DR63 has the appropriate composition to serve as the enriched component for the younger WGSC and could represent a portion of the northern part of the Galápagos plume not sampled south of the WGSC. Similar compositions to samples from volcanic cone DR63 have been found in the northern part of the 11-14 Ma Galápagos hotspot track offshore Costa Rica, indicating that this composition is derived from the northern portion of the Galápagos plume. The older WGSC requires involvement of an enriched mantle two (EMII) type source, not recognized thus far in the Galápagos system, and is interpreted to reflect entrained material either from small-scale heterogeneities within the upper mantle or from the mantle transition zone. Overall the source material for the 0-1.5 Ma WGSC ocean crust appears to represent mixing of depleted upper mantle with Northern Galápagos Plume material of relatively uniform composition in relatively constant proportions.

1 Introduction

Geochemical anomalies along mid-ocean ridges near hotspot systems that form ocean islands and seamounts (e.g., Iceland, Azores, Tristan, Galápagos) have been interpreted to reflect interaction between mantle plumes and mid-ocean ridges (e.g., Schilling, 1973; Schilling et al., 1982; Hanan et al., 1986; Schilling, 1991). One of the paramount examples of plume-ridge interaction is flow of Galápagos plume material to the adjacent Galápagos Spreading Center (GSC), also known as the Cocos-Nazca Spreading Center since it lies at the boundary of the Cocos and Nazca Plates. The Galápagos Archipelago and hotspot tracks on the northeast-moving Cocos Plate, consisting of the Cocos aseismic ridge and related seamount province to the north, and on the eastward-moving Nazca Plate, including Carnegie, Malpelo and Coiba aseismic ridges are the surface expressions of the long-lived Galápagos mantle plume and its interaction with the GSC over the last 23 Ma (Fig. 1; e.g., Handschumacher, 1976; Hey and Vogt, 1977; Wilson and Hey, 1995; Canales et al., 1997; Werner et al., 1999, 2003). Over the last 5 Ma, the GSC, located north of the Galápagos hotspot, has been progressively drifting northwards but has been repeatedly captured by the hotspot, as reflected by numerous ridge-jumps (Wilson and Hey, 1995; Mittelstaedt et al., 2012; Gibson et al., 2015).

Based on geophysical and geochemical data, as well as numerical and laboratory studies, a large variety of plume-ridge interaction models have been proposed to describe the transport of Galápagos plume material towards the GSC and the distribution of the plume signal along the ridge axis over ~1,000 km. These models are broadly divided into 1) transport to the GSC along channels within the base of the lithosphere (e.g., Morgan, 1978; Schilling et al., 1982; Verma and Schilling, 1982; Braun and Sohn, 2003); 2) deflection of the Galápagos plume head primarily eastwards due to eastward migration of the Nazca Plate but with some of the material in the north reaching the ridge axis (Richards and Griffiths, 1989; Geist,

1992; White et al., 1993; Harpp and White, 2001); 3) gravity driven plume dispersal along the base of the lithosphere (Bercovici and Lin, 1996; Hoernle et al., 2000); 4) radial outflow of plume material away from its stem along the base of the lithosphere to the spreading center (Schilling et al., 2003; Shorttle et al., 2010); 5) subsolidus transport of plume material beneath a viscous residual plug to the ridge (Kokfelt et al., 2005; Ito and Bianco, 2014; Villagomez et al., 2014; Byrnes et al., 2015); and 6) melt transport via veins and channels below the anhydrous peridotite solidus (Gibson et al., 2015).

Modern seafloor bathymetry and geochemistry identify two regions of maximum plume influence along the GSC at c. 92°W and 90.5°W separated by the 91°W transform. Both areas are characterized by axial high morphology, increased crustal thickness (up to 8-9 km; Ito and Lin, 1995; Canales et al., 2002; Mittelstaedt et al., 2014) and excursions in various geochemical plume signals (Schilling et al., 2003; Christie et al 2005; Kokfelt et al., 2005; Ingle et al., 2010; Gibson et al., 2015). Recent seismic tomographic studies of the upper mantle, extending to depths of up to 400 km beneath the Galápagos archipelago, reveal flow of plume material towards the GSC (Villagómez et al., 2014 and references therein). The observed low-velocity seismic anomaly beneath the archipelago can be interpreted to represent an upwelling mantle plume located between ~90.5 to 91.5°W that bends northwards at depths below the hydrous peridotite solidus (>100 km). Although low resolution of the available seismic array does not explicitly identify plume material reaching the GSC, a general inference can be made that plume material is transported to the western and eastern GSC consistent with maximum plume signals west and east of the 91°W transform. Bending of the plume to the north rather than the east (direction of Nazca Plate motion) is likely to reflect capture of the GSC as it migrated over the plume (Gibson et al., 2015).

At the Western GSC (WGSC), possible surface expressions of plume transport towards the GSC are several arcuate chains of volcanic seamounts and islands (up to ~1.8 Ma old) in the western inside corner of the 91°W transform of which the most widely known is the Wolf-Darwin Lineament (Morgan, 1978; White et al., 1993; Sinton et al., 1996; Harpp and Geist, 2002; Mittelstaedt et al., 2012). These arcuate volcanic chains radiate from Pinta Island northwestwards until they intersect the WGSC at 91°00'W, 91°16'W, 91°47'W and 92°10'W (Sinton et al., 2003). Ages of the lineaments relative to the underlying ocean crust south of the WGSC are however largely unresolved.

Our study addresses temporal variations in the influx of Galápagos plume material into the melt generation zone of the WGSC at the 92°W axial high over a period of 1.5 Ma. During the R/V SONNE 208 cruise, we sampled a c. 50 km long, northward-trending profile from the WGSC ridge axis at ~91°56'W, 2°07'N to ~91°48'W, 2°32'N off axis (Fig. 1). All samples are situated within 8 km of the center profile line, except DR69 and DR72, which are located 17 and 23 km east of the profile line respectively. The profile was collected north of the spreading center to avoid overprinting by younger volcanism as is evident from the numerous volcanic edifices between the Galápagos Platform and the WGSC, largely clustered along the lineaments described above (Harpp and Geist, 2002; Sinton et al. 2003; Mittelstaedt et al., 2012). A further advantage of the sampled profile is that there is no evidence for ridge jumps or overlapping spreading centers along the 50 km profile. In addition, R/V Atlantis cruise AT15-63 (GRUVEE) carried out a detailed sampling (recovering 167 samples; http://www.soest.hawaii.edu/gruvee/sci/gruvee-samples.html) along the ridge axis with the Alvin submersible at the beginning of our profile (between 92°01'W and 91°51'W), characterized as a high magma supply area (Canales et al.,

2002; Detrick et al., 2002; Sinton et al., 2003; Cushman et al., 2004; Colman et al., 2012).

Here we report geochemical analyses (major and trace elements and radiogenic Sr-Nd-Pb isotope ratios) primarily of volcanic glass but also some whole rock samples, where no glass could be obtained, in order to constrain the temporal geochemical variations in plume-ridge interaction along a restricted length of the WGSC at one of the major locations of present-day plume influx into the ridge.

2 Geologic Setting of the Sample Area

The sampling profile extends from 91°57′W, 02°07′N at the WGSC ridge crest to 91°36′W, 02°32′N off-axis. It covers 50 km of ocean crust lacking morphological evidence for significant amounts of off-axis volcanism (Fig. 1b). The NNE striking profile lies between the two westernmost arcuate volcanic lineaments that approach the WGSC from the South (e.g., Sinton et al., 2003). The ridge crest at 92°W is characterized by axial high morphology, cut by a 10-40 m deep axial summit graben and is inferred to be associated with high magma supply enhanced by presumable influx of Galápagos plume material (Canales et al., 2002; Detrick et al., 2002; Sinton et al., 2003; Cushman et al., 2004; Colman et al., 2012). Beneath the spreading axis, a melt lens has been seismically imaged at ~1.6 km depth (Blacic et al., 2004). Colman et al. (2012) and McClinton et al. (2013; 2015) provide a detailed geological map of this High Magma Supply (HMS) area along with the geochemical characterization of individual lava units.

The area north of the ridge axis (to about 02°12'N) is characterized by well-defined abyssal hills morphology, e.g. alternating ridge and valley type structures, oriented sub-parallel to the ridge axis with the basins reaching depths of 2,000 m below sea level (b.s.l.). Further to the north (between 02°12' and 02°32'N), variations

in the morphology become progressively less pronounced due to increased sediment cover, but are nevertheless clearly visible in the bathymetry (Fig. 1b). Most abyssal hills have relatively steep south-facing scarps but gentle northward dipping slopes made up of multiple short scarps, consistent with a tectonic control for the formation of the abyssal hill morphology. The depth of the individual basins progressively increases to the north as the seafloor regionally subsides, reaching a maximum depth of 2,600 m b.s.l. at the northernmost end of the mapped area.

An east-west striking array of conical edifices has been mapped at 2°18'N between the profile line and sample locations DR69 and DR72 to the east (Fig. 1b). They have diameters of up to c. 1 km at their base and elevations c. 250 m above the surrounding seafloor (Fig. 1c). We interpret them to result from low-volume, off-axis volcanism, as a result of recovering volcanic material at the cone at location DR63 about 23 km north of the spreading axis (hereafter referred to as Seamount 63; inverted triangle in Fig. 1b). Overall the volume of off-axis volcanic cones in the mapped area north of the WGSC is very small compared to south of the WGSC. Using half-spreading rates of 30 km/Ma for the last 1.4 Ma and 32 km/Ma for crust generated more >1.4 Ma ago (Mittelstaedt et al., 2012), the profile covers ~1.5 Ma of ocean crust formation. No fossil ridges (remaining after a ridge jump) or obvious overlapping spreading centers have been identified along the sampling profile. In this context, the intact morphology of Seamount 63 indicates formation north of the spreading axis within the past 0.76 Ma.

3. Sample Background and analytical methods

This study focuses on samples obtained by dredging at 21 sites with the German research vessel SONNE during cruise SO208 in July/August 2010 from ocean crust formed at the WGSC (Fig. 1b). Additional samples from on-axis

seamount 45 (Fig. 1b) and off-axis seamount 63 (Fig. 1c) were also analyzed as they represent discrete volcanic centers. Seamount 63 sits on the existing ocean crust and shows no sign of having been dissected, as is the case with the split seamount at 89°32'W along the eastern GSC (Christie et al., 2005, figure 8). Therefore this seamount is likely to have sampled parts of the off-axis melt column to the north of the WGSC.

The recovered samples comprise pillow and sheet lava fragments, often with fresh glass rims up to several centimeters thick. An extended description of the sample treatment and analytical procedures, along with data tables for major and trace element reference material, are presented in Herbrich et al. (2015) and summarized below. A correlated table with all data and sample coordinates is provided in Table A1.

From the 21 dredge hauls, major element compositions were mostly obtained on fresh glass chips (n = 60) using the JEOL JXA-8200 Electron Microprobe (EPMA) at GEOMAR. Based on multiple analysis of RM VG-A99, VG-2 and Scapolite, reproducibility is below 3% RSD for SiO_2, Al_2O_3, MgO, FeO, CaO, Na_2O, K_2O,TiO_2 and SO_2, except 6.2% RSD for P_2O_5 and 20.2% RSD for MnO. Accuracy of the standards relative to reference values of Jarosewich et al. (1980) is better than 2%, except MnO (12.2%). Major element compositions of nine additional whole rock samples were determined by X-Ray Fluorescence Analysis (XRF) on fused pellets using a Magix Pro PW 2540 XRF at the Institute of Mineralogy and Petrography at the University of Hamburg. Accuracy of most elements for JGB-1, JB-3, JB-2, JA-3, JG-3 and JG-2 reference materials lies within 3% of the preferred GeoReM values (http://georem.mpch-mainz.gwdg.de/); measured values are provided in Table A2.

Trace element concentrations of glass chips and whole rock samples were determined by laser ablation (LA) and solution inductively coupled plasma mass

spectrometry (ICP-MS) at the Institute of Geoscience, University of Kiel. The setup uses an Agilent 7500cs quadrupole ICP-MS for dissolved samples and a Coherent GeoLasPro Plus 193 nm Excimer laser connected to a second Agilent 7500cs instrument. LA-ICPMS used five spot analyses per sample at 80 µm beam diameter and of 10 Hz repetition rate with a total acquisition time of 80 s for each shot. BCR-2G and MPI-DING RM's (KL-2G, St.HS. 6/80-G, GOR128-G and GOR132-G; Jochum et al., 2006) were repeatedly measured along with samples as unknowns. Detailed information on reproducibility and accuracy of the standards relative to GeoRem values is provided in Table A3. Duplicate analyses of samples on average deviated less than 5% (range 1-8%) except Cs (16%). Sample digestion procedure for solution ICP-MS followed the method described in Garbe-Schönberg (1993). Reproducibility based on separate digestions was usually better than 4% RSD for reference materials and 5% RSD for samples. The accuracy of BIR-1, BHVO-2 and BCR-2 lies within 3% of the preferred GEOREM values (http://georem.mpch-mainz.gwdg.de/); data is provided in Table A4.

Radiogenic isotope ratios of Sr, Nd and Pb of glass and whole rock samples were analyzed by thermal ionization mass spectrometry (TIMS) at GEOMAR. Prior to digestion in a hot HF:HNO_3 mixture, chips of glass and whole rock were leached in 2 N HCl at 70°C for one hour and repeatedly rinsed in 18.2 MΩ/cm H_2O thereafter. Element separation followed the method described in Hoernle et al. (2008). A Finnigan MAT262 RPQ^{2+}, operating in static multi-collection mode was used to determine Pb isotope ratios, which were mass bias corrected applying the ^{207}Pb-^{204}Pb double spike (DS) technique of Hoernle et al. (2011). DS corrected NBS981 values (n = 36) and associated 2σ external errors (2SD) yielded $^{206}Pb/^{204}Pb$ = 16.9413 ± 0.0024, $^{207}Pb/^{204}Pb$ = 15.4988 ± 0.0025, $^{208}Pb/^{204}Pb$ = 36.7236 ± 0.0063, $^{207}Pb/^{206}Pb$ = 0.914849 ± 0.000037 and $^{208}Pb/^{206}Pb$ = 2.167693 ± 0.000097 over the

course of the study. Sr and Nd isotopic ratios were measured on a Thermo Scientific TRITON, operating in static multi-collection mode. Within-run normalization used $^{86}Sr/^{88}Sr = 0.1194$ and $^{146}Nd/^{144}Nd = 0.7219$. Sample data are reported relative to NBS987 for $^{87}Sr/^{86}Sr$ (0.710250 ± 0.000010, 2SD, n = 63) and relative to La Jolla for $^{143}Nd/^{144}Nd$ (0.511850 ± 0.000007; 2SD; n = 45) and our in-house Nd monitor Spex for $^{143}Nd/^{144}Nd$ (0.511715 ± 0.000006; 2SD; n = 38). Replicate analyses for Pb, Sr and Nd isotopic composition by means of separate sample digests (n = 7) were reproduced within 2SD obtained for the above-mentioned standards.

4 Results

Inspection of the glasses under a binocular microscope and thin sections of the crystallized matrix of whole rock samples along with volatile-free major element sums of 99.07 ± 0.38 wt% (1SD, n = 60) for glass and 99.5 ± 0.2 wt% (1SD, n = 9) for whole rocks samples (Table A1) indicate that the analyzed samples have undergone only minimal alteration. Petrographically we find no evidence for alteration in the glass samples. Petrographic study of a representative suite of whole rock samples (n = 32) covering the entire profile varies from fresh to moderately altered with increasing distance from the ridge axis and thus presumably with increasing age. Due to the absence of fresh glass at several locations, we analyzed the freshest whole rocks for nine out of the 32 whole rock samples. Signs of alteration in the whole rocks include 1) the formation of palagonite and iron oxides, 2) alteration rinds around pillow rims and halos along cooling cracks, 3) partial filling and lining of vesicles with calcite and secondary minerals or with very thin Mn coatings, and 4) formation of Mn crusts up to 1-2 cm thick. Such material was, however, avoided during handpicking to obtain the freshest material possible for analyses. The vast majority of the sampled material is pyroxene- and/or plagioclase-bearing lava. Rare

olivine, spinel and Fe-Ti-oxide (magnetite, ilmenite) phenocrysts are present in some samples. Seamount 63 was the only location where highly vesicular (40-45% vesicles) lava with 1-2% fresh olivine phenocrysts was recovered. As will be shown in more detail in section 4.3, the data set is subdivided into three groups that primarily differ in radiogenic isotope composition and estimated formation ages: 1) WGSC basement 0-30 km (0-1.0 Ma) from the ridge axis, including an on-axis seamount (circles and triangle respectively), 2) WGSC basement 30-50 km (1.0-1.5 Ma) away from the ridge axis (squares) and 3) Seamount 63 sample (<0.76 Ma, inverted triangle).

4.1 Major element compositions

On the total alkali versus silica (TAS; Fig. 2; Le Maitre et al., 1989) diagram, the samples range from tholeiitic basalt to basaltic andesite (Fig. 2) with SiO_2 = 48.5-53.5 wt.% and MgO = 2.9-8.8 wt%. Their Mg-numbers (Mg# = mol[Mg/(Mg+Fe^{2+})]) vary from 0.62 to 0.24, reflecting relatively primitive (off-axis Seamount 63 with MgO = 8.8 wt.% and off-axis ocean crust sample DR56-2_wr with MgO = 8.3 wt.%) to evolved (DR72 and DR74 off-axis ocean crust samples with MgO of 2.9 and 4.4 wt.% respectively) basaltic compositions.

Major element contents plotted against MgO form reasonably well-defined trends consistent with shallow level magma differentiation for ocean crust samples formed at the WGSC (Fig. 3). In general, SiO_2, FeO^T ($\sum$Fe as FeO), TiO_2, P_2O_5, Na_2O and K_2O increase while CaO and Al_2O_3 decrease with decreasing MgO. These observations are typical for the differentiation of tholeiitic melts and consistent with fractionation of the observed phenocryst assemblage of olivine + plagioclase + clinopyroxene. The on-axis DR45 tholeiitic seamount samples (triangles) fall on the trend formed by the <30 km WGSC basement (circles). The >30 km WGSC ocean

crust basement samples (squares) overlap with the <30 km WGSC basement in SiO_2, CaO, FeO^T, Al_2O_3 but deviate to lower TiO_2, P_2O_5 and Na_2O with decreasing MgO. Basaltic andesite lavas from both groups (DR72, 0-30 km WGSC basement and DR74, 30-50 km WGSC basement) show the greatest deviation of Na_2O and TiO_2 from the fractionation array consistent with fractionation of Ti-bearing phases (e.g., ilmenite) and more albite-rich plagioclase during advanced stages of melt differentiation. The shallower trend for P_2O_5 and TiO_2 in the 0-30 km WGSC group points to different mineral proportions, greater amounts of apatite and Fe-Ti oxide fractionation, leading to different bulk solid/melt partition coefficients for these oxides. Seamount 63, the most mafic tholeiite of the entire sample suite, lies at the primitive end of the inferred fractionation lines for FeO^T and Na_2O, but is shifted towards higher TiO_2, P_2O_5 and K_2O and lower CaO and Al_2O_3 values at the mafic end of the fractionation line, formed by the majority of sampled ocean crust basement samples.

On MgO versus CaO and Al_2O_3 diagrams (Fig. 3), the majority of WGSC basement samples plot within the High Magma Supply (HMS) field of present-day ridge axis between 92°05'-91°51'W (Colman et al., 2012; yellow part of the GSC in Fig. 1a, dark gray field in Fig. 2 and 3), which marks the southern (young) end of the off-axis sampling profile. On the MgO versus Al_2O_3 plot, only one whole rock sample that does not plot in the HMS field plots within the Low Magma Supply area (LMS of Colman et al., 2012; see Fig. 1a) field, located at the 95°04'-94°48'W propagating rift. On the MgO versus SiO_2, TiO_2, Na_2O, K_2O and P_2O_5 diagrams, the most mafic (MgO >7.5 wt.%) basement samples fall largely in the LMS field. We note that large variations in MgO exist in samples of similar age (e.g., 2.9 to 9.0 wt% at 2.3°N), but such large variations in MgO are not observed in the LMS reference data and lavas from there are restricted to mafic compositions. Nevertheless, the obvious discrepancies to the present HML field indicate that the proportions of fractionating

minerals may have varied in the axial magma reservoir over the past 1.5 Ma. In addition, fluctuations in melting processes and source compositions may have caused changes in parental melt composition.

4.2 Trace elements

Primitive-mantle-normalized trace element patterns of the 0-30 km WGSC group (Fig. 4a) are similar to enriched mid-ocean ridge basalt (E-MORB) patterns of present-day WGSC in the 92°W area (e.g., Ingle et al 2010 and references therein). Highly to moderately incompatible trace element concentrations fall between those found in lavas 1) from the Northern Galápagos Islands (Wolf, Darwin, Pinta; http://georoc.mpch-mainz.gwdg.de/georoc/) and the northernmost Cocos Ridge and Seamount Province to its NW, located offshore Costa Rica (Werner et al. 2003; Harpp et al. 2005), and 2) WGSC normal-mid-ocean-ridge basalt (N-MORB) at >95.5°W. The WGSC at >95.5°W does not appear to be influenced by the Galápagos plume and thus is thought to represent local upper mantle (e.g., Ingle et al., 2010). The least incompatible elements, including the heavy rare earth elements (HREE), Y and Ti, display a very slight negative slope (e.g., $(Sm/Yb)_n$ = 1.0-1.4). The patterns for the on-axis DR45 seamount are similar to the other 0-30 km group samples, but have higher overall concentrations reflecting the evolved nature of these lavas (Fig. 4a). The pattern for primitive off-axis Seamount 63 lava (Fig. 4a) cross cuts the other patterns in heavy to intermediate rare earth elements, Zr, Hf, Ti and Y because the least incompatible elements form a steep negative slope. The seamount sample also has the highest highly incompatible element abundances, excluding the most evolved basement samples. The pattern for Seamount 63 lava has ocean-island-basalt (OIB)-type geochemical characteristics and mimics the lower boundary of the field for the Northern Galápagos Islands (see Fig. 4a). The 30-50 km WGSC basement samples

(Fig. 4b) have similar trace element abundances as the <30 km WGSC basement, displaying E-MORB-type geochemical characteristics. The most evolved samples in both age groups (DR 74 and DR72) have the most enriched incompatible element abundances of the ocean crust samples, with the exception that they have more pronounced negative Sr and Ti anomalies as a result of increased plagioclase and Ti-oxide fractionation.

Incompatible element ratios plotted versus distance from the WGSC ridge axis do not show any systematic variations with distance (and thus age) over the entire profile. Variations in ratios at single locations, however, are significant, but show a range similar to that observed along the present ridge axis (not shown).

On the Nb/Yb versus Th/Yb discrimination diagram (Fig. 5; after Pearce, 2008), the ocean crust profile samples form a tight and well-correlated positive array. The WGSC basement samples including those from the on-axis seamount DR45 plot within the MORB-OIB array close to reference for E-MORB. The off-axis Seamount DR63 data is shifted towards OIB compositions (Fig. 5a). On the Nb/Yb versus TiO_2/Yb discrimination diagram, the ocean crust samples, excluding DR72, plot in the shallow melting MORB array (Fig. 5b). The most evolved samples (DR72 and DR74) have lower TiO_2/Yb than the other samples reflecting Fe-Ti oxide fractionation. Seamount 63 samples plot in the tholeiitic field of the deep melting OIB array.

4.3 Isotopic data

Variations in Sr, Nd and Pb isotope ratios are fairly limited for each group. The 0-30 km ocean crust group has $^{87}Sr/^{86}Sr$ = 0.70291-0.70307, $^{143}Nd/^{144}Nd$ = 0.51298-0.51302, $^{206}Pb/^{204}Pb$ = 18.82-19.09, $^{207}Pb/^{204}Pb$ = 15.56-15.60, $^{208}Pb/^{204}Pb$ = 38.58-38.94. The 30-50 km ocean crust group overlaps or extends to slightly more extreme values compared to the <30 km group ($^{87}Sr/^{86}Sr$ = 0.70309-0.70324 (excluding DR72

whole rock; see below), $^{143}Nd/^{144}Nd$ = 0.51296-0.51299, $^{206}Pb/^{204}Pb$ = 18.95-19.02, $^{207}Pb/^{204}Pb$ = 15.59-15.62, $^{208}Pb/^{204}Pb$ = 38.84-39.01).

On plots of distance from the spreading axis vs. isotope ratio (Fig. 6), the <30 km WGSC samples show no systematic variation with distance from the ridge axis and therefore also not with age of the crust to 1.0 Ma. The <30 km WGSC basement samples form an inverse correlation on the $^{87}Sr/^{86}Sr$ versus $^{143}Nd/^{144}Nd$ and $^{206}Pb/^{204}Pb$ versus $^{143}Nd/^{144}Nd$ isotope ratio plots (Fig. 7+8c) and positive correlations on $^{206}Pb/^{204}Pb$ versus $^{207}Pb/^{204}Pb$ and $^{208}Pb/^{204}Pb$ correlation diagrams (Fig. 8a-b). Including the on-axis seamount samples, the <30 km group falls between N-MORB from the WGSC at >95.5°W (Ingle et al., 2010) and enriched Galápagos Archipelago lavas.

In contrast to the <30 km basement samples, the >30 km WGSC samples have more radiogenic $^{87}Sr/^{86}Sr$ (Fig. 7) and extend to more radiogenic $^{207}Pb/^{204}Pb$ and $^{208}Pb/^{204}Pb$ and to less radiogenic Nd isotopic compositions compared to the <30 km group samples with similar $^{206}Pb/^{204}Pb$ ratios (Fig. 8). With increasing distance from the ridge (or with increasing age from 1.0 Ma to 1.5 Ma), the $^{87}Sr/^{86}Sr$, $^{207}Pb/^{204}Pb$ and $^{208}Pb/^{204}Pb$ ratios of the WGSC crust slightly increase while $^{143}Nd/^{144}Nd$ slightly decreases. Although the spatial and temporal trends are subtle, they are outside analytical errors and thus may be significant if representative of the 1.0-1.5 Ma crust formed at the WGSC.

Seamount 63 samples have more enriched isotopic compositions than the underlying WGSC basement, displaying more radiogenic $^{87}Sr/^{86}Sr$ = 0.70335 and $^{206}Pb/^{204}Pb$ = 19.55, $^{207}Pb/^{204}Pb$ = 15.66, $^{208}Pb/^{204}Pb$ = 39.60 and less radiogenic $^{143}Nd/^{144}Nd$ = 0.51288. The Seamount 63 samples have higher $^{207}Pb/^{204}Pb$ and $^{208}Pb/^{204}Pb$ for a given $^{206}Pb/^{204}Pb$ than any known sample from the present-day Galápagos Archipelago (Galápagos Islands and associated submarine volcanism).

5 Discussion

At mid-ocean ridges new magma from the mantle emerges constantly, creating new oceanic crust, which spreads away from the ridge as newer crust is formed. Therefore the age of the crust generally increases with increasing distance from the ridge axis. Complications with this simple model can arise for example from ridge jumps or from extensive off-axis volcanism (e.g., Brandl et al., 2012). While off-axis volcanism played only a very minor role in crust formation north of the WGSC (Fig. 1a-c), ridge jumps are likely in the vicinity of hotspots as they are able to capture the ridge (e.g., Mittelstaedt et al., 2012; Gibson et al., 2015). There is however no obvious evidence for ridge jumps or overlapping spreading centers in the sampled area from the bathymetry or from synthetic magnetic anomaly profiles (Mittelstaedt et al., 2012).

5.1 Melting conditions

Incompatible element geochemistry can be used to assess the relative melting conditions of the ocean crust and seamount samples. The TiO_2/Yb ratio (Fig. 5b) can provide information about deep vs. shallow melting (Pearce, 2008). On the Nb/Yb vs. TiO_2/Yb plot, all WGSC basement and the on-axis seamount samples (DR45) plot in the MORB array, pointing towards shallow melting, while the off-axis seamount samples (DR63) have higher TiO_2/Yb plotting in the tholeiitic portion of the deep melting OIB array. Since Ti is fractioned from Yb by garnet, the elevated ratios of Seamount 63 samples indicate residual garnet in the source of the seamount lavas. The nearly flat HREE patterns (e.g., $(Sm/Yb)_n = 1.0\text{-}1.4$ and $(Tb/Yb)_n = 1.0\text{-}1.2$; where n indicates normalization to primitive mantle) of the ocean crust basement samples are also consistent with garnet being largely absent in the integrated melt column

residuum. Only Seamount 63 samples with steep HREE patterns (e.g., $(Sm/Yb)_n$ = 2.4 and $(Tb/Yb)_n$ = 1.5) show evidence for having formed in the presence of residual garnet. Based on the steep HREE patterns taken together with the elevated ratios of more to less incompatible elements (e.g., (Nb/Yb) = ~11.5, (Th/Yb) = ~0.8 and $(La/Yb)_n$ = ~5.8), the off-axis Seamount 63 lavas appear to have formed at greater depth and by lower degrees of melting than the ocean crust basement samples formed on the spreading center axis. Since the seamount shows no evidence of having been split, it must have formed off-axis, north of the WGSC, in a near-ridge but intraplate setting.

Despite trace element evidence for WGSC lavas being largely generated in the spinel stability field, U-series disequilibria of zero age lavas throughout the GSC require melt initiation in the garnet stability field (Kokfelt et al., 2005). The absence of a garnet signature (based on REE and TiO_2) in the samples at the GSC most likely is the combined effect of high degrees of melting of a trace element depleted source upwelling to shallow depths. Melting with garnet in the residuum causes fractionation of U-Th and thus U-series disequilibria. Although this occurs at the bottom of the melt column (≥50-60 km considering that both garnet peridotite and pyroxenite could be in the source; Hirschmann and Stolper, 1996), ^{230}Th–^{238}U disequilibria remains largely unchanged by shallower melting. Significant deviations from initial disequilibria can only be generated through extended magma residence times and crustal assimilation. In conclusion, geochemical evidence suggests that melting of the WGSC source took place over a large depth range from ≥50-60 to ~10 km (the present crustal thickness at 92°W; Ito and Lin, 1995; Canales et al., 2002; Mittelstaedt et al., 2014). In contrast, melts forming Seamount 63 were generated at greater depth primarily within the garnet stability field (≥50-60 km).

5.2. Geochemical variations with age

Plots of distance from the ridge axis versus incompatible elements and/or isotope ratios provide information about the geochemical evolution at the ridge axis over time and reveal temporal fluctuations in material input or changes in melt parameters, e.g., degree of melting. No systematic variations in either incompatible element ratios (not shown) or isotope ratios, however, were observed in the 0-30 km group samples (Fig. 6). Variations within the 30-50 km WGSC sample group lie largely within the range of the recent WGSC lavas, reflecting only minor variations in the proportions of isotopically enriched and depleted source materials over the last 1.0 Ma for most of the samples.

The limited data set for the >30 km WGSC basement samples defines a very crude trend towards higher $^{87}Sr/^{86}Sr$, $^{207}Pb/^{204}Pb$, and $^{208}Pb/^{204}Pb$ and lower $^{143}Nd/^{144}Nd$ compositions with increasing distance from the ridge, indicating involvement of an additional enriched component. With decreasing age from ≥1.5 to 1.0 Ma, this source appears to have been slowly replaced by source material similar to the <1.0 Ma lavas. We note, however, that the present data set is too limited to fully explore compositional changes in the WGSC source beyond 1.0 Ma. The limited data set reflects the difficulty in obtaining samples of off-axis crust through dredging with increasing distance from the ridge axis, due to more subdued abyssal hills morphology and the high sediment accumulation rates (2 g cm^{-2} $ka^{-}1$; Mitchell, 1998). The nature of the additional enriched component in the >30 km WGSC basement samples, however, is explored further below using isotope correlation diagrams.

5.3. The role of plume-ridge interaction in generating the geochemical compositions of the 0-1.5 Ma WGSC lavas

We now use the radiogenic Sr-Nd-Pb isotope ratios to determine to what extent Galápagos plume material has influenced the chemistry of the magmas forming the oceanic crust at the WGSC over the last 1.5 Ma. Studies of the trace element and isotope geochemistry of the Galápagos lavas show that the archipelago is geochemically zoned with an enriched east-facing, horseshoe-shaped region enclosing a depleted region in its inner part (e.g., White and Hofmann, 1978; Geist et al., 1988; White et al., 1993; Harpp and White, 2001). The enriched horseshoe-shaped region shows regional heterogeneity in isotopic composition (White et al., 1993; Hoernle et al., 2000; Harpp and White, 2001). White et al. (1993) noted that the northern and southern portions of the enriched region displayed distinct isotopic compositions.

Using the data of White et al. (1993), it was shown that the enriched horseshoe-shaped region could be subdivided into four distinct geochemical domains: enriched Northern (NGD), Central (CGD) and Southern (SGD) Galápagos domains and an inner depleted Eastern Galápagos Domain (EGD) (Hoernle et al., 2000). The relative geographic position of the enriched domains has remained constant over the last ~20 Ma (Hoernle et al., 2000; 2002; Werner et al., 2003; Geldmacher et al., 2003), leading to the proposition that the Galápagos plume is geochemically zoned. It was further proposed that the plume taps distinct reservoirs in its source area near the core-mantle boundary and preserves these geochemical heterogeneities through laminar flow, which then leads to a spatially zoned hotspot track. Kerr and Meriaux (2004) confirmed that distinct geochemical reservoirs in a plume's source area can generate an azimuthally zoned plume, which will produce an asymmetric geographical distribution of geochemical compositional domains in the erupted hot spot lavas, as not only seen at the Galápagos hotspot but also at the Hawaiian, Marquesas and Society island chains.

In an attempt to identify the number of distinct end members involved in generating the compositional variations seen at the Galápagos, Harpp and White (2001) performed principal component analysis using Sr, Nd, Pb and He isotope ratios. They concluded that the Galápagos isotopic geochemistry could be explained by mixing of four distinct end members (shown in Fig. 7 and 8): 1) Wolf-Darwin (WD), 2) Plume (PL), 3) Floreana (FLO) and 4) Depleted Galápagos or Upper Mantle (DGM or DUM). Principal component analysis however is strictly only applicable to linear systems and there are limitations to this approach when applied to non-linear systems, such as radiogenic isotopes of different elements (e.g., Rudge et al., 2013). A comparison of the Pb versus Pb (Fig. 8a-b) with the Pb versus Nd isotope diagram (Fig. 8c) illustrates one of the problems with the principal component analysis end members. On the Pb versus Pb isotope diagrams, the Wolf-Darwin (WD) end member plots closer to the Northern Galápagos Domain (NGD) reference field, while the Plume (PL) end member plots closer to the Central Galápagos Domain (CGD) reference field (isotope data from White et al., 1993, is used to define the reference fields). On the Pb versus Nd isotope diagram, however, the relative location of the end members is opposite with the WD end member plotting closer to the Central Galápagos Domain field and the PL end member plotting closer to the Northern Galápagos Domain field. Due to the limitations of evaluating the combined Sr-Nd-Pb isotope data set with principal component analysis, we will not consider the principal component analysis end members further in this study.

Despite largely plotting within the compositional range of Galápagos lavas, the samples from the WGSC profile, however, also cannot be consistently explained as mixtures of specific Galápagos Archipelago reference domains. On all isotope correlation diagrams, the <1.0 Ma samples form a crude array that can be explained by mixing of enriched and depleted end members. On the Sr-Nd and Pb-Nd

diagrams, the Central Galápagos Domain could serve as the enriched end member, but this is not consistent with the Pb-Pb isotope diagrams, where the enriched end of the array trends into the Northern Galápagos Domain. The >1.0 Ma group also does not provide a consistent picture in respect to the Galápagos Archipelago domains. On the Sr-Nd isotope diagram, all the >1.0 Ma samples plot within the Central Galápagos Domain, but on the Pb-Pb and Pb-Nd isotope diagrams, the data largely plots between the Northern Galápagos Domain and MORB. Below we will discuss other potential end members for generating the arrays for both WGSC basement age groups and if these enriched end members are derived from the Galápagos hotspot.

5.3.1 Mixing relationships for the younger WGSC (<30 km group)

Along the Western Galápagos Spreading Center, three groups of MORB (Normal, Transitional and Enriched) have been identified, based on their compositional and morphological characteristics (e.g., Schilling et al., 1983; Sinton et al., 2003; Cushman et al., 2004; Ingle et al., 2010). With increasing distance from the 91°W Transform Fault, the morphology of the ridge changes from axial high to axial valley type character, mirrored by a change in geochemical composition from E-MORB (91.0-92.7°W) to Transitional (T)-MORB (92.7-95.5°W) to N-MORB (95.5-98°W; Detrick et al., 2002; Sinton et al., 2003; Ingle et al., 2010). Along our profile north of 92°W, we primarily found E-MORB type compositions in the samples from <30 km off axis group. These data overlap the on-axis E-MORB field. Several samples however plot within the T-MORB field on the Pb-Pb and Pb-Nd plots. Therefore the chemical composition of the lavas produced on the ridge at ~92°W have remained relatively constant for the last ~1.0 Ma, although in some instances more depleted compositions were erupted in the past.

The systematic westward decrease in degree of geochemical enrichment along the WGSC is generally attributed to a diminishing supply of Galápagos plume material to the spreading center with increasing distance from the hotspot. It is a matter of ongoing discussion, whether the decreasing plume signal reflects radial outflow of plume material along the base of the lithosphere into the spreading center at various locations (Schilling et al., 2003; Shorttle et al., 2010). Alternatively, it could reflect input of plume material into the GSC west and east of the 91°W Transform Fault followed by lateral flow and dilution of plume material as it flows beneath the ridge axis to the west and east, i.e. away from the 91°W Transform Fault (e.g., Kokfelt et al., 2005; Ingle et al., 2010; Gibson, et al., 2015). Finally, a combination of both alternatives has also been proposed (e.g., Geldmacher et al., 2013). Regardless of the route that plume material takes to get to the ridge and whether or not it flows laterally beneath the ridge, the enriched material appears to become systematically diluted through mixing with depleted upper mantle farther from the plume. Therefore it seems highly likely that the source of the geochemical anomaly is related to the Galápagos Hotspot.

The Sr-Nd-Pb isotopic ratios from the 0-30 km WGSC basement samples form reasonably well-correlated arrays on isotope diagrams (Fig. 7-8), which lie roughly between the fields of local GSC N-MORB from >95.5°W, an area thought to be uninfluenced by contributions from the Galápagos plume (Ingle et al., 2010) and enriched components. Although the obvious source for the enriched components is the Galápagos hotspot, none of the previously identified Galápagos Archipelago geochemical domains or principal component analysis end members can alone serve as the enriched end member on all isotope diagrams, as discussed in the preceding section.

The material reaching the WGSC over the last 1.0 Ma appears to have a distinct composition from the sampled seamounts and islands within the Northern Galápagos Domain just to the south of the WGSC. In contrast to Galápagos Archipelago volcanism, Seamount 63 has an appropriate composition to serve as the enriched end member on all isotope correlation diagrams (Fig. 7-8). A simplified melt mixing line between Seamount 63 and possible N-MORB from the WGSC between 95.5 and 98°W (Ingle et al., 2010) passes through the <30 km WGSC group samples on all isotope plots. Mixing parameters are provided in Table A5. Subtle differences in isotopic composition and Sr-Nd-Pb concentrations of the mixing components can explain the variability of the younger WGSC array.

Since Seamount 63 does not plot within any of the Galápagos Archipelago domains, there is some question as to whether this is a plume composition or represents a long-lived heterogeneity in the upper mantle north of the Galápagos hotspot, which would place the entire question of plume-ridge interaction along the WGSC into question. Interestingly, however, samples from the northern part of the 11-15 Ma old Galapagos Hotspot Track (Seamount Province located north of the Cocos Ridge) overlap the Northern Galápagos Domain field but extend to more radiogenic Pb and less radiogenic Nd isotope compositions (Fig. 9). Based on the similar composition of the northern, central and southern parts of the 11-15 Ma Galápagos hotspot track offshore of Costa Rica and northern, central and southern parts of the western Galápagos Archipelago, it has been proposed that the Galápagos plume has been geochemically zoned for at least the last 15 Ma (Hoernle et al., 2000; Werner et al., 2003; Geldmacher et al., 2003) and that the older Northern Domain (Seamount Province) lavas display a larger isotopic heterogeneity than documented by the Northern Galápagos Archipelago lavas. Notably Seamount 63 plots within or on the boundary of the paleo Northern Galápagos Domain field,

consistent with the Seamount 63 source and the enriched component in the 0-1.0 Ma WGSC group samples being derived from the Galápagos plume. Evidence for the existence of the Northern Domain signature before 15 Ma has been found in Cocos Plate ocean crust (Geldmacher et al., 2013) and seamount samples on the Cocos Plate offshore Nicaragua (Herbrich et al., 2015). Evidence for the unique Northern Galapagos Domain signature has even been found in young arc volcanism from Central Costa Rica to Central Nicaragua, reflecting recycling of >15 Ma Northern Domain material subducted beneath Costa Rica and possibly Nicaragua (Hoernle et al., 2008; Gazel et al., 2009). In conclusion, the mantle from the northern portion of the Galápagos plume reaching the WGSC over the last 1.5 Ma (see below for discussion of 1.0-1.5 Ma WGSC lavas) has a distinct composition from the volcanism in the Pliocene-Quaternary Northern Galápagos Archipelago, but is similar in composition to lavas from the older Galápagos hotspot track.

In conclusion, simplified binary mixing calculations indicate that the array formed by the 0-30 km WGSC off-axis crust can be generated by mixing an enriched Northern Galápagos Domain component similar to Seamount 63 with GSC N-MORB and/or a depleted plume component. The similarity of the composition of Seamount 63 and lavas from the northern part of the 11-15 Ma Galápagos hotspot track provides evidence that Galápagos plume material is indeed feeding the WGSC and that the composition of the Quaternary northern Galápagos plume is more heterogeneous than previously recognized from sampling of the northern Galápagos Archipelago. These results provide further evidence supporting the long-term zonation of the Galapagos hotspot (Hoernle et al., 2000; Werner et al., 2003; Geldmacher et al., 2013; Herbrich et al., 2015).

5.3.2 Mixing relationships for the older WGSC (30-50 km group)

Only samples from four locations between 30-50 km from the WGSC were recovered with fresh glass from three sites and whole rocks from the fourth. Compared with the younger WGSC samples, the older WGSC samples become more enriched with increasing distance from the ridge axis and thus presumably with increasing age between 1.0-1.5 Ma ago. On the isotope correlation diagrams (Fig. 7-8), the older (>30 km) WGSC off-axis group samples deviate from the field of the younger (<30 km) WGSC basement, extending to more radiogenic $^{207}Pb/^{204}Pb$, $^{208}Pb/^{204}Pb$ and less radiogenic $^{143}Nd/^{144}Nd$ isotope ratios at a given $^{206}Pb/^{204}Pb$ along with overall higher $^{87}Sr/^{86}Sr$. As noted above, the >30 km group also does not have a composition that consistently plots in a single Galápagos Archipelago Domain. On the Pb isotope diagrams, the two samples taken furthest from the WGSC have higher $^{207}Pb/^{204}Pb$ and $^{208}Pb/^{204}Pb$ than Galápagos samples with similar $^{206}Pb/^{204}Pb$. The excellent linear array ($r^2 = 0.99$) for $^{207}Pb/^{204}Pb$ versus $^{208}Pb/^{204}Pb$, as well as crude positive correlations of $^{87}Sr/^{86}Sr$ with $^{207}Pb/^{204}Pb$ and $^{208}Pb/^{204}Pb$ confirms that these samples are trending from the <30 km array towards a different enriched component and that the range in $^{87}Sr/^{86}Sr$ is not simply a reflection of seawater alteration or assimilation of seawater altered crust (Fig. 7).

It should be noted that DR74-1 and DR68-1 are the two most evolved samples in the >30 km group (and the second and third most evolved samples from the 92°W north profile) and therefore assimilation of local sediments (<1.0 Ma old sediments from IODP Site 1256, Höfig, 2014) and/or Mn crusts (GMAT 14D; Frank et al., 1999) by melts with compositions similar to samples from the <30 km group could conceivably cause an increase in $^{87}Sr/^{86}Sr$, $^{207}Pb/^{204}Pb$ and $^{208}Pb/^{204}Pb$ and decrease in $^{143}Nd/^{144}Nd$. Binary mixing on the Pb isotope diagrams should form a straight line; however, it is not possible to put a straight line from one of the <30 km group samples through the >30 km group samples with the highest $^{208}Pb/^{204}Pb$ to local

sediments. On the Pb isotope diagrams, mixing of a composition on the mixing line between the <30 km group and the Seamount 63 sample with local sediments (or manganese crusts) could explain the elevated $^{207}Pb/^{204}Pb$ and $^{208}Pb/^{204}Pb$ ratios of the >30 km group. Mixing of Seamount 63 with local sediments (or Mn crusts), however, will not go through the data on the Sr-Nd and Pb-Nd diagrams, because both end members have lower Nd isotopic composition that the >30 km WGSC data. Therefore we cannot explain the composition of the older group samples with addition of crustal components. A possible explanation to generate the unique chemical compositions of the >30 km group samples is mixing of 1) mantle material/melt with a similar composition to the <30 km group samples with 2) an Enriched Mantle (EM) II type component with elevated $^{207}Pb/^{204}Pb$, $^{208}Pb/^{204}Pb$ and $^{87}Sr/^{86}Sr$, lower $^{143}Nd/^{144}Nd$ but similar $^{206}Pb/^{204}Pb$ isotope ratios compared to the <30km group.

An EMII-like component that could serve as the enriched component for the >30 km WGSC off-axis crust has not been reported previously for the Galápagos Archipelago (e.g., White et al., 1993; Harpp and White, 2001), the GSC (Schilling et al., 2003; Ingle et al., 2010) or the hotspot tracks (Hoernle et al., 2000; Werner et al., 2003). In contrast to Seamount 63, the EMII-like source does not plot within one of the Galápagos domain arrays (including data from the archipelago and the hotspot tracks) on the Pb isotope diagrams. Therefore, there is some question as to whether this component is intrinsic to the Galápagos plume, i.e. derived from the plume source. Alternatively, it could reflect a random heterogeneity in the upper mantle beneath the ridge or could be upper, transition-zone or lower mantle material entrained by the plume during ascent. As is indicated by off-axis seamounts (e.g., Brandl et al. 2012), Petit Spot volcanoes (Machida et al., 2009; 2015), Pliocene volcanism on Christmas Island (Hoernle et al., 2011) and the isolated Godzilla

seamount (Geldmacher et al., 2008), enriched components are present in the uppermost asthenospheric mantle and are tapped by low-degree melting in intraplate settings. Although the available data of 1.0-1.5 Ma WGSC off-axis crust are too few to constrain fully the origin and extent of the observed EMII flavor, we do however note that a component similar to samples from the <30 km group serve as one mixing component for the >30 km group. Therefore similar components were tapped beneath the WGSC over the last 1.5 Ma with the addition of an EMII-type component in lavas older than 1.0 Ma.

5.4. Model for plume-ridge interaction over the last ~1.5 Ma

Seismic tomography of the upper mantle beneath the Galápagos Archipelago shows that the low-velocity anomaly associated with the Galápagos plume rises into the upper mantle beneath the westernmost islands but bends to the north at a depth of ~100 km between ~90-92°W (Villagómez et al., 2014). Although the presently available tomography doesn't resolve the anomaly north of 1°N latitude, it is likely that the northern part of the plume extends to the WGSC located at ~2°N.

The two groups of seafloor lavas formed over the last ~1.5 Ma along and north (Seamount 63) of the WGSC have distinct compositional characteristics compared to lavas from the Galápagos Archipelago and Hotspot Tracks. The <1.0 Ma WGSC basement lavas, however, can be explained by stirring together of melts from a Seamount 63 source with melts from a depleted upper mantle (or possibly depleted plume) source. The similarity of Seamount 63 compositions to 11-15 Ma old lavas from the northern portion of the Galápagos Hotspot Track (or the Seamount Province located north of the Cocos Ridge) offshore Costa Rica suggest that the Seamount 63 source material is derived from the northern part of the Galápagos plume, even though it is compositionally distinct from the northern Galápagos Archipelago lavas

erupted south of the WGSC. The bathymetry of Seamount 63 clearly indicates that it was not formed on the ridge axis, but slightly north of it, or spreading processes would have split it. The geochemistry points to generation of these isotopically-enriched lavas through lower degrees of melting at deeper depths than the isotopically-depleted <1.0 Ma WGSC lavas. The WGSC lavas were formed through larger degrees of melting to shallower depths, resulting in a greater dilution of the enriched melts from the plume material by depleted melts from the upper mantle and/or plume.

Eruption of plume-derived melts north of the WGSC, even though the plume was located south of the spreading center, indicates that some plume material must have been able to flow at sub-solidus depth slightly north of the ridge axis before it upwelled far enough to cross its solidus, melted and the melt ascended to the surface. Further research on low volume off-axis seamounts in plume-ridge interaction settings on the plume-free side of the spreading axis is needed to constrain more fully the flow paths of plume material near spreading centers.

Concerning the change in composition of the seafloor lavas at c. 1.0 Ma, it is worth noting that a ridge jump has been proposed at 1.0 Ma for the Eastern Galápagos Spreading Center (EGSC; Mittelstaedt et al., 2012). Although there is no evidence for a ridge jump in the available magnetic data from profiles north of and perpendicular to the WGSC, the ridge jump east of the 91°W Transform Fault may have somehow also influenced mantle flow to the west of the transform fault, causing a change in the source material feeding the WGSC. If the subtle temporal evolution in geochemistry from 1.5 to 1.0 Ma is correct, then the change from EMII-type signatures to the <1.0 Ma composition along the WGSC took place over ≥0.5 Ma. Therefore a ridge jump at ~1.0 Ma along the EGSC cannot alone explain the temporal geochemical evolution of the WGSC between 1.5-1.0 Ma. Since no

evidence for an EMII-like component in the Galápagos Archipelago or the hotspot tracks has been found thus far, we do not believe that the EMII-type component is intrinsic to the plume and suggest that it was entrained along the northern margin of the plume or was a local heterogeneity within the upper mantle.

In Figure 10, we show a schematic illustration of the geochemical evolution of plume-ridge interaction along the WGSC over the last 1.5 Ma. At 1.5 Ma, the WGSC was located closer to the Galápagos hotspot and sampled low volume domains of EMII-like mantle (yellow; 30-50 km basement), possibly entrained by the upwelling plume (Fig. 10a) or randomly distributed within the upper mantle. The ridge migrated away from the hotspot to the north at a half-spreading rate of ~32 km/Ma until 1.4 Ma, at which time the half spreading rate to the north of the ridge decreased to ~30 km/Ma (Mittelstaedt et al., 2012). At ≤1.4 Ma, the composition of the ocean crust formed at the WGSC began changing in composition towards that of the <1.0 Ma (<30 km) WGSC basement lavas. At 1.0 Ma, the EMII-like component was exhausted. Thereafter the lava composition remained relatively constant reflecting binary mixing of N-MORB with material from the northern part (Northern Domain) of the Galápagos mantle plume with a composition similar to that of Seamount 63 (Fig. 10b). Some of the plume mantle was able to pass beneath the ridge at sub-solidus depth and melt within the garnet stability field. Low-degree adiabatic melting of this mantle north of the WGSC produced Seamount 63 with a more enriched plume-like isotopic composition. Melts from plume material, which upwelled and melted beneath the ridge, were stirred together with melts from upwelling depleted mantle that formed at shallow depths beneath the ridge. Magmatism along the Wolf-Darwin and other arcuate lineaments to the south of the WGSC has a slightly different composition from the material erupted at the WGSC over the last ≤1.4 Ma. Therefore the Quaternary Northern Galápagos Domain is more heterogeneous than previously

thought but similar in composition to melts derived from the northern part of the Galápagos hotspot 11-15 Ma ago, providing further support that the Galápagos hotspot is compositionally zoned (Hoernle et al., 2000; Werner et al., 2003; Geldmacher et al., 2003; Kerr and Meriaux, 2004).

6 Summary and Conclusions

This is the first study to present a detailed profile of the ocean crust extending from a ridge axis (Western Galápagos Spreading Center or WGSC) to ~50 km off-axis with a sampling interval of generally <5 km but in all cases <10 km, allowing assessment of the temporal evolution in geochemistry of plume-ridge interaction. Using half-spreading rates from paleomagnetic data, we estimate that the ocean crust sampled along this profile formed over ~1.5 Ma. Three distinct compositional groups can be identified: 1) Tholeiitic to basaltic andesitic ocean crust samples dredged from the ridge axis and from the flanks of abyssal hills (0-30 km from the WGSC ridge axis with ages of 0-1.0 Ma), show no systematic variations in geochemistry with distance from the ridge axis or with age. 2) Primitive tholeiitic basalts from a small off-axis volcanic cone (Seamount 63), which formed north of the spreading axis at <0.76 Ma have a more enriched isotopic composition than the basement lavas. 3) Tholeiitic to basaltic andesitic basement samples dredged from abyssal scarps located 30-50 km from the ridge axis (~1.0-1.5 Ma) display increasing Sr and Pb isotope ratios and decreasing Nd isotope ratios with increasing distance from the spreading center (and thus also increasing age).

All basement samples (0-1.5 Ma) have incompatible element abundances and isotopic compositions intermediate between enriched Galápagos plume domains and N-MORB from the GSC at >95.5°W. Nevertheless, these samples cannot simply be explained through mixing of a single Galápagos compositional domain, such as the

Northern Galápagos Archipelago Domain located just south of the WGSC, with a depleted N-MORB component. Seamount 63, however, has the appropriate Sr-Nd-Pb isotopic composition to serve as the enriched component for the <1.0 Ma samples. Mixtures of seamount 63 melts with N-MORB melts, similar in composition to lavas sampled at >95.5°W along the WGSC that show no evidence of plume-ridge interaction, can explain the data arrays formed by the <1.0 Ma old basement samples. Interestingly, no data has been published thus far from the Galápagos Archipelago with a Pb and Nd isotopic composition similar to the Seamount 63 samples. Lavas from the northern part of the 11-15 Ma Galápagos Hotspot Track offshore Costa Rica (Seamount Province north of the Cocos Ridge) have similar compositions to Seamount 63. Therefore Seamount 63 is likely to come from the northern part of the Galápagos plume, providing additional support that zonation of the Galápagos plume can be traced back into the middle Miocene. The 30-50 km group samples indicate the presence of an additional enriched component with an enriched mantle (EM) II like isotopic flavor in the ridge axis melt column between 1.0-1.5 Ma ago. This type of component has not been found either in the Galápagos Archipelago or the hotspot tracks (Cocos, Carnegie, Malpelo and Coiba Ridges and Seamount Province north of Cocos Ridge) thus far. Therefore we believe it may have been a batch of EMII material entrained by the rising Galápagos plume or a compositional heterogeneity within the upper mantle at that time.

In conclusion, the differences in the composition of the on-ridge to ~50 km off-ridge samples (0-1.5 Ma) cannot simply be explained by mixing Quaternary Galápagos Archipelago compositions with different amounts of upper MORB source mantle. Instead, greater heterogeneity is required in the northern portion of the zoned Quaternary Galápagos plume than previously recognized, containing compositions similar to lavas erupted 11-15 Ma ago from the northern portion of the Galápagos

plume. The 1.0-1.5 Ma old lavas also required the presence of a second enriched (EMII-like) component, which we believe to be derived from the transition zone or upper mantle beneath the WGSC.

Acknowledgements

This contribution is dedicated to the pioneering work of Fred Frey on the petrology and geochemistry of mantle derived melts at mid ocean ridges, hotspots and convergent plate margins, which have influenced the professional careers of KH and FH. We thank S. Hauff, M. Thöner and U. Westernströer for technical assistance during analytical work and the SO208 crew and Shipboard Scientific Parties for their support during the cruise. Special thanks go to M. Anders and P. Hoffmann for assistance with sample preparation and to M. Portnyagin, J. Geldmacher and T. Hansteen for fruitful discussions that helped to improve the manuscript. We also thank the government of Ecuador for granting permission to work in their territorial waters. Special thanks go to Denis Geist, Sally Gibson and an anonymous reviewer for their critical, in depth, but constructive evaluation, which helped to improve an earlier version of the manuscript. We are grateful for editorial handling and comments by Fred Frey, Marc Norman and Shichun Huang and their tremendous patience during the revision process. This study was supported by the German Federal Ministry of Education and Research (BMBF; Grant 03G0208A SO 208-PLUMEFLUX).

References

Bercovici, D. and Lin, J. (1996) A gravity current model of cooling mantle plume heads with temperature-dependent buoyancy and viscosity. Journal of *Geophysical Research* **101**, 3291-3309.

Blacic, T.M., Ito, G., Canales, J.P., Detrick, R.S. and Sinton, J. (2004) Constructing the crust along the Galápagos Spreading Center 91.3°–95.5°W: Correlation of seismic layer 2A with axial magma lens and topographic characteristics. *Journal of Geophysical Research* **109**, B10310.

Brandl, P.A., Beier, C., Regelous, M., Abouchami, W., Haase, K.M., Garbe-Schönberg, D. and Galer, S.J.G. (2012) Volcanism on the flanks of the East Pacific Rise: Quantitative constraints on mantle heterogeneity and melting processes. *Chemical Geology* **298-299**, 41-56.

Braun, M.G. and Sohn, R.A. (2003) Melt migration in plume-ridge systems. *Earth and Planetary Science Letters* **213**, 417-430.

Byrnes, J.S., Hooft, E.E.E., Toomey, D.R., Villagómez, D.R., Geist, D.J. and Solomon, S.C. (2015) An upper mantle seismic discontinuity beneath the Galápagos Archipelago and its implications for studies of the lithosphere-asthenosphere boundary. *Geochemistry, Geophysics, Geosystems* **16**, 1070-1088.

Canales, J.P., Dañobeitia, J.J., Detrick, R.S., Hooft, E.E., Bartolomé, R. and Naar, D.F. (1997) Variations in axial morphology along the Galápagos spreading center and the influence of the Galápagos hotspot. *Journal of Geophysical Research* **102**, 27341-27354.

Canales, J.P., Ito, G., Detrick, R.S. and Sinton, J. (2002) Crustal thickness along the western Galápagos Spreading Center and the compensation of the Galápagos hotspot swell. *Earth and Planetary Science Letters*, **203**, 311-327.

Christie, D.M., Werner, R., Hauff, F., Hoernle, K. and Hanan, B.B. (2005) Morphological and geochemical variations along the eastern Galápagos Spreading Center. *Geochemistry, Geophysics, Geosystems* **6**, Q01006.

Colman, A., Sinton, J.M., White, S.M., McClinton, J.T., Bowles, J.A., Rubin, K.H., Behn, M.D., Cushman, B., Eason, D.E., Gregg, T.K.P., Grönvold, K., Hidalgo, S., Howell, J., Neill, O. and Russo, C. (2012) Effects of variable magma supply on mid-ocean ridge eruptions: Constraints from mapped lava flow fields along the Galápagos Spreading Center. *Geochemistry, Geophysics, Geosystems* **13**, Q08014.

Cushman, B., Sinton, J., Ito, G. and Dixon, F.J. (2004) Glass compositions, plume-ridge interaction, and hydrous melting along the Galápagos Spreading Center, 90.5°W to 98°W. *Geochemistry, Geophysics, Geosystems* **5**, Q08E17.

Detrick, R.S., Sinton, J.M., Ito, G., Canales, J.P., Behn, M., Blacic,T., Cushman, B., Dixon, J.E., Graham, D.W. and Mahoney, J.J. (2002) Correlated geophysical, geochemical, and volcanological manifestations of plume-ridge interaction along the Galápagos Spreading Center. *Geochemistry, Geophysics, Geosystems* **3**, 8501.

Frank, M., Reynolds, B.C. and O'Nions, K.R. (1999) Nd and Pb isotopes in Atlantic and Pacific water masses before and after closure of the Panama gateway. *Geology* **27,** 1147-1150.

Garbe-Schönberg, C.-D. (1993) Simultaneous determination of thirty-seven trace elements in twenty-eight international rock standards by ICP-MS. *Geostandards Newsletter* **17**, 81-97.

Gazel, E., Carr, M. J., Hoernle, K., Feigenson, M. D., Szymanski, D., Hauff, F., and van den Bogaard, P. (2009) Galápagos-OIB signature in southern Central

America: Mantle refertilization by arc-hot spot interaction. *Geochemistry, Geophysics, Geosystems* **10**, Q02S11.

Geist, D.J., White, W.M. and McBirney, A.R. (1988) Plume-asthenosphere mixing beneath the Galápagos archipelago. *Nature* **333**, 657-660.

Geist, D.J. (1992) An appraisal of melting processes and the Galapagos Hotspot; major- and trace-element evidence. *Journal of Volcanology and Geothermal Research* **52**, 65-82.

Geldmacher, J., Hanan, B.B., Blichert-Toft, J., Harpp, K., Hoernle, K., Hauff, F., Werner, R. and Kerr, A.C. (2003) Hafnium isotopic variations in volcanic rocks from the Caribbean Large Igneous Province and Galápagos hot spot tracks. *Geochemistry, Geophysics, Geosystems* **4**, 1525-2027.

Geldmacher, J., Hoernle, K., Klügel, A., van den Bogaard, P., and Bindeman, I. (2008) Geochemistry of a new enriched mantle type locality in the northern hemisphere: Implications for the origin of the EM-I source. *Earth and Planetary Science Letters* **265**, 167-182.

Geldmacher, J., Höfig, T.W., Hauff, F., Hoernle, K., Garbe-Schönberg, D. and Wilson, D.S. (2013) Influence of the Galápagos hotspot on the East Pacific Rise during Miocene superfast spreading. *Geology* **41**, 183-186.

Gibson, S. A., Geist, D. J., and Richards, M. A. (2015) Mantle plume capture, anchoring, and outflow during Galápagos plume-ridge interaction. *Geochemistry, Geophysics, Geosystems* **16**, 1634-1655.

Hanan, B.B., Kingsley, R.H., and Schilling, J.G. (1986) Pb isotope evidence in the South Atlantic for migrating ridge-hotspot interactions: *Nature* **322**, 137–144.

Handschumacher, D.W., (1976) Post-Eocene Plate Tectonics of the Eastern Pacific, The Geophysics of the Pacific Ocean Basin and its Margin. American Geophysical Union, pp. 177-202.

Harpp, K. and Geist, D., (2002) Wolf-Darwin lineament and plume-ridge interaction in northern Galápagos. *Geochemistry, Geophysics, Geosystems* **3**, 8504.

Harpp, K.S., Wanless, V.D., Otto, R.H., Hoernle, K. and Werner, R. (2005) The Cocos and Carnegie Aseismic Ridges: A Trace Element Record of Long-term Plume-Spreading Center Interaction. *Journal of Petrology* **46**, 109-133.

Harpp, K.S. and White, W.M. (2001) Tracing a mantle plume: Isotopic and trace element variations of Galápagos seamounts. *Geochemistry, Geophysics, Geosystems* **2**, 1042.

Herbrich, A., Hoernle, K., Werner, R., Hauff, F., Bogaard, P. v. d., and Garbe-Schönberg, D. (2015) Cocos Plate Seamounts offshore NW Costa Rica and SW Nicaragua: Implications for large-scale distribution of Galápagos plume material in the upper mantle. *Lithos* **212–215**, 214-230.

Hey, R. and Vogt, P. (1977) Spreading center jumps and sub-axial asthenosphere flow near the Galápagos hotspot. *Tectonophysics* **37,** 41-52.

Hirschmann, M. M. and Stolper, E. M. (1996) A possible role for garnet pyroxenite in the origin of the "garnet signature" in MORB. *Contributions to Mineralogy and Petrology* **124**, 185-208.

Hoernle, K., Abt, D.L., Fischer, K.M., Nichols, H., Hauff, F., Abers, G.A., Bogaard, P. v. d., Heydolph, K., Alvarado, G., Protti, M. and Strauch, W. (2008) Arc-parallel flow in the mantle wedge beneath Costa Rica and Nicaragua. *Nature* **451**, 1094-1097.

Hoernle, K., Hauff, F., Kokfelt, T.F., Haase, K., Garbe-Schönberg, D. and Werner, R. (2011) On- and off-axis chemical heterogeneities along the South Atlantic Mid-Ocean-Ridge (5-11°S): Shallow or deep recycling of ocean crust and/or intraplate volcanism? *Earth and Planetary Science Letters* **306,** 86-97.

Hoernle, K., Bogaard, P. v. d., Werner, R., Lissinna, B., Hauff, F., Alvarado, G. and Garbe-Schönberg, D. (2002) Missing history (16–71.0 Ma) of the Galápagos hotspot: Implications for the tectonic and biological evolution of the Americas. *Geology* **30,** 795-798.

Hoernle, K., Werner, R., Morgan, J.P., Garbe-Schönberg, D., Bryce, J. and Mrazek, J. (2000) Existence of complex spatial zonation in the Galápagos plume. *Geology* **28**, 435-438.

Höfig, T. W. (2014) Geochemical (major and trace elements and Sr-Nd-Hf-Pb isotopes) characterization of the upper oceanic crust (sediments to gabbros) at ODP/IODP Site 1256 in the eastern Central Pacific, *Ph.D. Dissertation*, Christian-Albrechts-Universität Kiel, Kiel, Germany, 147 pp.

Ingle, S., Ito, G., Mahoney, J.J., Chazey W.III, Sinton, J., Rotella, M. and Christie, D.M. (2010) Mechanisms of geochemical and geophysical variations along the western Galápagos Spreading Center. *Geochemistry, Geophysics, Geosystems* **11,** Q04003.

Ito, G. and Lin, J. (1995) Oceanic spreading center-hotspot interactions: Constraints from along-isochron bathymetric and gravity anomalies. *Geology* **23,** 657-660.

Ito, G.T. and Bianco, T. (2014) Patterns in Galápagos magmatism arising from the upper mantle dynamics of plume-ridge interaction, In The Galápagos: A Natural Laboratory for the Earth Sciences (ed. Harpp, K.S., Mittelstaedt, E., d'Ozouville, N. Graham, D.W), *Geophysical Monograph Series*, AGU, Washington, D. C., pp 245–262.

Jarosewich, E., Nelen, J. A., and Norberg, J. A. (1980) Reference Samples for Electron Microprobe Analysis. *Geostandards Newsletter* **4**, 43-47.

Kerr, R.C. and Mériaux, C. (2004) Structure and dynamics of sheared mantle plumes. *Geochemistry, Geophysics, Geosystems* **5**, Q12009.

Kokfelt, T.F., Lundstrom, C., Hoernle, K., Hauff, F. and Werner, R. (2005) Plume-ridge interaction studied at the Galápagos spreading center: Evidence from ^{226}Ra-^{230}Th-^{238}U and ^{231}Pa-^{235}U isotopic disequilibria. *Earth and Planetary Science Letters* **234**, 165-187.

Le Maitre, R.W., Bateman, P., Dudek, A., Keller, J., Lameyre, J., Le Bas, M., Sabine, P., Schmidt, P.A., Sorensen, R., Streckeisen, H., Woolley, A. and Zanettin, B. (1989). A Classification of Igneous Rocks and Glossary of Terms, Recommendations of the International Union of Geological Sciences, Subcomission on the Systematics of Igneous Rocks. *A classification of ingeous rocks and glossary of terms: Recommendations of the International Union of Geological Sciences Subcommission on the Systematics of ingeous rocks*. Blackwell Scientific. Oxford. GB.

MacDonald, G.A., and Katsura, T. (1964) Chemical Composition of Hawaiian Lavas1. *Journal of Petrology* **5**, 82-133.

Machida, S., Hirano, N., and Kimura, J.I. (2009) Evidence for recycled plate material in Pacific upper mantle unrelated to plumes. *Geochimica et Cosmochimica Acta* **73**, 3028-3037.

Machida, S., Hirano, N., Sumino, H., Hirata, T., Yoneda, S., and Kato, Y. (2015) Petit-spot geology reveals melts in upper-most asthenosphere dragged by lithosphere. *Earth and Planetary Science Letters* **426**, 267-279.

McClinton, J.T., and White, S.M. (2015) Emplacement of submarine lava flow fields: A geomorphological model from the Niños eruption at the Galápagos Spreading Center. *Geochemistry, Geophysics, Geosystems* **16**, 899-911.

McClinton, J.T., White, S.M., Colman, A., and Sinton, J.M. (2013) Reconstructing lava flow emplacement processes at the hot spot-affected Galápagos

Spreading Center, 95°W and 92°W. *Geochemistry, Geophysics, Geosystems* **14,** 2731-2756.

Mitchell, N.C. (1998) Sediment accumulation rates from Deep Tow profiler records and DSDP Leg 70 cores over the Galápagos spreading center. In Geological Evolution of Ocean Basins: Results From the Ocean Drilling Program (ed. A. Cramp et al.), Geological Society, London, Special Publications 131, 199-209.

Mittelstaedt, E., Soule, S., Harpp, K., Fornari, D., McKee, C., Tivey, M., Geist, D., Kurz, M.D., Sinton, C. and Mello, C. (2012) Multiple expressions of plume-ridge interaction in the Galápagos: Volcanic lineaments and ridge jumps. *Geochemistry, Geophysics, Geosystems* **13,** Q05018.

Mittelstaedt, E., Soule, A., Harpp, K.S. and Fornari D. (2014) Variations in crustal thickness, plate rigidity and volcanic processes throughout the northern Galápagos volcanic province, In The Galápagos: A Natural Laboratory for the Earth Sciences (ed. Harpp, K.S., Mittelstaedt, E., d'Ozouville, N. Graham, D.W), Geophysical Monograph Series, AGU, Washington, D. C., pp. 263–284.

Morgan, W.J. (1978) Rodriguez, Darwin, Amsterdam, ..., A second type of Hotspot Island. *Journal of Geophysical Research: Solid Earth* **83**, 5355-5360.

O'Neill, H.StC. (1981) The transition between spinel lherzolite and garnet lherzolite, and its use as a Geobarometer. *Contributions to Mineralogy and Petrology* **77**, 185-194.

Pearce, J. A. (2008) Geochemical fingerprinting of oceanic basalts with applications to ophiolite classification and the search for Archean oceanic crust: *Lithos* **100**, 14-48.

Richards, M.A. and Griffiths, R.W. (1989) Thermal entrainment by deflected mantle plumes. *Nature* **342**, 900-902.

Rudge, J. F., Maclennan, J., and Stracke, A. (2013) The geochemical consequences

of mixing melts from a heterogeneous mantle. *Geochimica et Cosmochimica Acta* **114**, 112-143.

Schilling, J.G. (1991) Fluxes and excess temperatures of mantle plumes inferred from their interaction with migrating mid-ocean ridges. *Nature* **352**, 397-403.

Schilling, J.G. (1973) Iceland Mantle Plume: Geochemical Study of Reykjanes Ridge. *Nature* **242**, 565-571.

Schilling, J.G. (1991) Fluxes and excess temperatures of mantle plumes inferred from their interaction with migrating mid-ocean ridges. *Nature* **352**, 397-403.

Schilling, J.G., Fontignie, D., Blichert-Toft, J., Kingsley, R. and Tomza, U. (2003) Pb-Hf-Nd-Sr isotope variations along the Galápagos Spreading Center (101°-83°W): Constraints on the dispersal of the Galápagos mantle plume. *Geochemistry, Geophysics, Geosystems* **4**, 8512.

Schilling, J.G., Kingsley, R.H. and Devine, J.D. (1982) Galápagos Hot Spot-Spreading Center System 1. Spatial Petrological and Geochemical Variations (83°W–111°W). *Journal of Geophysical Research* **87**, 5593–5610.

Shorttle, O., Maclennan, J., and Jones, S.M. (2010) Control of the symmetry of plume-ridge interaction by spreading ridge geometry. *Geochemistry, Geophysics, Geosystems* **11,** Q0AC05.

Sinton, C.W., Christie, D.M., and Duncan, R.A. (1996) Geochronology of Galápagos seamounts. *Journal of Geophysical Research* **101**, 13689-13700.

Sinton, J., Detrick, R., Canales, J.P., Ito, G. and Behn, M. (2003) Morphology and segmentation of the western Galápagos Spreading Center, 90.5°-98°W: Plume-ridge interaction at an intermediate spreading ridge. *Geochemistry, Geophysics, Geosystems* **4**, 8515.

Verma, S.P. and Schilling, J.-G. (1982) Galápagos Hot Spot-Spreading Center System: 2. $^{87}Sr/^{86}Sr$ and large ion lithophile element variations (85°W-101°W). *Journal of Geophysical Research: Solid Earth* **87**, 10838-10856.

Villagómez, D.R., Toomey, D.R., Geist, D.J., Hooft, E.E.E. and Solomon, S.C. (2014) Mantle flow and multistage melting beneath the Galápagos hotspot revealed by seismic imaging. *Nature Geoscience* **7**, 151–156.

Werner, R., Hoernle, K., Bogaard, P.v.d., Ranero, C., Huene, R.v.d., Korich, D. (1999) A drowned 14 Ma old Galápagos Archipelago off the coast of Costa Rica: Implications for evolutionary and tectonic models. *Geology* **27**, 499-502.

Werner, R., Hoernle, K., Barckhausen, U. and Hauff, F. (2003) Geodynamic evolution of the Galápagos hot spot system (Central East Pacific) over the past 20 m.y.: Constraints from morphology, geochemistry, and magnetic anomalies. *Geochemistry, Geophysics, Geosystems* **4**, 1108.

White, S. (2015). Galápagos region multibeam bathymetry compilation, 97°W-86°W (investigator Scott White). Integrated Earth Data Applications (IEDA). http://doi.org/10.1594/IEDA/321842

White, W. M., and Hofmann, A. W. (1978) Geochemistry of the Galápagos Islands: implications for mantle dynamics and evolution. In *Year Book Carnegie Inst. Washington* **77**, 596-606.

White, W.M., McBirney, A.R. and Duncan, R.A. (1993) Petrology and Geochemistry of the Galápagos Islands: Portrait of a Pathological Mantle Plume. *Journal of Geophysical Research* **98**, 19533-19563.

Wilson, D.S. and Hey, R.N. (1995) History of rift propagation and magnetization intensity for the Cocos-Nazca spreading center. *Journal of Geophysical Research* **100,** 10041-10056.

Figure Captions

Figure 1: a) Bathymetric map of the Eastern Pacific area including all major morphological features (GSC refers to Galápagos Spreading Center, also commonly referred to as the Cocos-Nazca Spreading Center). During cruise SO208 Leg 2 an off-axis "Profile 1" was sampled by dredging north of the western (W)GSC being separated from the eastern (E)GSC by the 91°W Transform Fault. The purple and yellow part of the WGSC axis marks the High and Low Magma Supply (HMS and LMS respectively) Area after Colman et al. (2012). The red box shows the location of figure b. b) Detailed bathymetric map of the WGSC off-axis profile based on multibeam bathymetric data with sample locations (circles). Map contains bathymetric data collected on R/V SONNE cruise SO208 combined with data from other cruises in this region (White, 2015, data DOI: http://doi.org/10.1594/IEDA/321842). c) Three dimensional visualization of off-axis volcanic cone DR63 and dredge track along its southwestern flank. The base diameter is ~1 km and elevation ~250 m above the surrounding seafloor. The intact conical form indicates that it formed north of the spreading axis rather than on the spreading axis or it would have been split in half by seafloor spreading as is observed along the EGSC (Christie et al., 2005, figure 8).

Figure 2: Silica versus total alkali diagram (after Le Maitre et al., 1989) of glass and whole rock (denoted with a "+" within the symbol) samples from the WGSC off-axis profile. Alkali basalt/tholeiite division after MacDonald & Katsura (1964); HMS – High Magma Supply area and LMS – Low Magma Supply area of the WGSC located at 92°05'-91°51'W and 95°04'-94°48'W respectively after Colman et al. (2012). Recent GSC on-axis data are from Christie et al. (2005), Cushman et al. (2004), and Schilling et al. (1982).

Figure 3: Diagrams of MgO versus major element oxides for the WGSC off-axis profile compared with WGSC on-axis samples showing typical tholeiitic fractionation trends formed by shallow fractionation of olivine, plagioclase and clinopyroxene. HMS – High Magma Supply area and LMS – Low Magma Supply area after Colman et al. (2012). Recent GSC on-axis field between 83-101°W contains data from Christie et al. (2005), Colman et al. (2012), Cushman et al. (2004), and Schilling et al. (1982).

Figure 4: Primitive-mantle-normalized multi-element diagrams. a) 0-1.0 Ma WGSC crust samples lie between WGSC N-MORB from >95.5°W and the Northern Galápagos Domain (NGD). Off-axis seamount sample DR63 (doted line) has similar incompatible element abundances to samples in the lower part of the NGD field, but cross-cuts the <1.0 Ma WGSC E-MORB-type patterns, indicating lower degrees of melting (highly incompatible element abundances similar to the most differentiated <1.0 Ma WGSC samples) at greater depth, i.e. with residual garnet (low abundances HREE and Y and negative slope of the least incompatible elements on the right hand side of the diagram). The flat HREE parts of the patterns for samples from the evolved on-axis cone DR45 compared to the negative slope of the HREE part of the patterns for the primitive off-axis cone (DR63) indicate that the melts feeding the off-axis cone formed by lower degrees of melting at deeper depths (in the garnet stability field) than the on-axis cone. b) Incompatible element patterns of 1.0-1.5 Ma WGSC crust samples are similar to those of the <1.0 Ma WGSC crust samples. In both diagrams the most evolved samples (DR72 and DR74) have the highest incompatible element abundances. Data for the NGD are from Harpp et al. (2005), Harpp and White (2001), Hoernle et al. (2000) and White et al. (1993). Data for WGSC >95.5°W are from Ingle et al. (2010).

Figure 5: Nb/Yb versus a) Th/Yb and b) TiO_2/Yb after Pearce (2008). a) All WGSC samples and the on- and off-axis seamounts plot within the MORB-OIB array. The younger (0-30 km; 0-1.0 Ma) and older (30-50 km; 1.0-1.5 Ma) WGSC crust samples overlap and form a tight array with E-MORB composition. Seamount 63, however, has higher Nb/Yb and Th/Yb ratios and plots near ocean island basalts (OIB). b) Nb/Yb versus TiO_2/Yb provides a good proxy to distinguish between shallow and deep melting. In the presence of garnet in the source, Yb will be retained. Melts formed at greater depths in the presence of residual garnet (such as OIBs) have higher TiO_2/Yb and plot above the MORB array, as is the case with Seamount 63 samples. The WGSC basement samples and the on-axis seamount (DR45) plot in the MORB array, reflecting shallow melting. Evolved samples that fractionated Fe-Ti oxides, such as DR72 and DR74, have low TiO_2/Yb.

Figure 6: Sr-Nd-Pb isotopic variations along the WGSC profile from the spreading axis to 50 km off-axis. The basement samples that are <30 km from the WGSC axis show minor and no systematic variations, whereas the basement samples taken at >30 km from the WGSC axis trend towards more radiogenic Sr and Pb and less radiogenic Nd isotope ratios, indicating the presence of greater amounts of a different enriched source with increasing age. The gray bar symbolizes the WGSC ridge axis and the small open circles are data from Ingle et al. (2010) from the ridge axis between 91.3-92.5°W. Ages on the top x-axis were calculated using half-spreading rates of 30 km/Ma for the last 1.4 Ma and 32 km/Ma for lavas up to 1.5 Ma old (Mittelstaedt et al., 2012). E-MORB from the ridge axis between 91.36°W-92.52°W are from Ingle et al. (2010). 2SD error bars are smaller than symbol size. Open square with cross is a replicate analysis of whole rock with elevated $^{87}Sr/^{87}Sr$, indicating minor but detectable interaction with seawater derived Sr. Nd and Pb

isotope ratios however were unaffected by seawater interaction. Additional information is in Fig. 7 caption.

Figure 7: Sr versus Nd isotope correlation diagram. The samples from the profile north of and perpendicular to the present-day WGSC axis form discrete mixing arrays between the local N-, T- and E- MORB fields of Ingle et al. (2010) and the geographical Galápagos Plume Domains defined by Hoernle et al. (2000). The latter are referred to as the depleted Eastern (EGD) and enriched Central (CGD), Northern (NGD) and Southern (SGD) Galápagos Domains. Large diamonds designate the proposed mixing components of Harpp and White (2001) used for principle component analysis (Wolf-Darwin = WD and PLUME = PL). Arrows point towards Floreana (FLO) and depleted upper mantle (DUM). Thick dashed lines represent binary mixing assuming similar Sr/Nd element ratios. See text for a detailed evaluation of the application of compositional domains versus principle component analysis end members. The data array of the <1.0 Ma WGSC crust can be generated by simply binary mixing of depleted N-MORB melts (star) with Seamount 63 melts using the parameters in Table A5. Off-axis seamount data of Brandl et al. (2012) from a plume-free portion of the East Pacific Rise are shown to demonstrate the presence of enriched components in the upper mantle unrelated to the presence of mantle plumes (open diamonds). Open symbols with cross are replicate analysis of whole rock chips in which $^{87}Sr/^{86}Sr$ displays small but significant contributions of seawater derived Sr as indicated by the horizontal displacement to higher $^{87}Sr/^{86}Sr$ at similar $^{143}Nd/^{144}Nd$ isotope ratios. Samples taken between 30-50 km distance from the WGSC (1.0-1.5 Ma) form a well-correlated array towards higher $^{87}Sr/^{86}Sr$ than the 0-1.0 Ma crust, indicating contribution from second enriched component distinct in composition from the off-axis volcanic cone Seamount 63. Site 1256 sediment data (Höfig, 2014) and GMAT Mn-crust data (Frank et al., 1999) are also shown. Sr-Nd

concentrations of the virtual N-MORB have been slightly adjusted to similar Sr/Nd (c. 13 ± 1) to obtain simplified, straight mixing lines. For mixing parameters see Table A5.

Figure 8: $^{206}Pb/^{204}Pb$ versus (a) $^{207}Pb/^{204}Pb$, (b) $^{208}Pb/^{204}Pb$ and (c) $^{143}Nd/^{144}Nd$ isotope correlation diagrams using the same reference fields, principle component analysis endmembers and data sources as in Fig. 7. Simplified binary mixing of N-MORB (star) and off-axis volcanic cone DR63 using the parameters in Table A5 generates trajectories passing through the data arrays formed by the 0-1.0 Ma WGSC crust on all diagrams. The 30-50 km WGSC basement samples deviate from the 0-30 km WGSC basement array towards higher $^{207}Pb/^{204}Pb$, $^{208}Pb/^{204}Pb$ and lower $^{143}Nd/^{144}Nd$ for a given $^{206}Pb/^{204}Pb$. The elevated $^{207}Pb/^{204}Pb$ and $^{208}Pb/^{204}Pb$ ratios cannot be explained by assimilation of <1.0 Ma old sediments and Mn crusts. See text for further details.

Figure 9: $^{206}Pb/^{204}Pb$ versus $^{208}Pb/^{204}Pb$ and $^{143}Nd/^{144}Nd$ isotope discrimination diagrams after Hoernle et al. (2000) show the Galápagos domains of today's Archipelago (fields with dashed lines) and the 11-15 Ma Galápagos hotspot track off Costa Rica, including the Cocos Ridge and Seamount Province to the north of it (fields with solid lines). Hoernle et al. (2000) and Werner et al. (2003) propose that the similar (although not identical) composition of the northern, central and southern parts of the Galápagos Archipelago and Hotspot Tracks reflects long-term (≥20 Ma) striped geochemical zonation of the Galápagos hotspot. Seamount 63 lavas have similar compositions to the lavas from the northern part (Northern Galápagos Domain – NGD) of the 11-15 Ma Galápagos hotspot track, suggesting that these seamount lavas were derived from the northern part of the Quaternary Galápagos plume. CGD = Central Galápagos Domain, SGD = Southern Galápagos Domain and EGD =

Eastern Galápagos Domains as defined by Hoernle et al. (2000) using data from White et al. (1993).

Figure 10: Conceptual model illustrates the temporal evolution of plume-ridge interaction at ~91°50'W of the Western Galápagos Spreading Center (WGSC) for (A) 1.5-1.0 Ma and (B) since 1.0-0 Ma. The N-S oriented profiles extend from the center of the Galápagos plume to north of the Western Galápagos Spreading Center (WGSC). Material erupting in the central (Central Galápagos Domain – CGD) and northern (Northern Galápagos Domain – NGD) parts of the Quaternary Galápagos Archipelago is derived from isotopically distinct plume sources (Hoernle et al., 2000). The composition of WGSC crust in both age groups can be explained through mixing of enriched Northern Galápagos Domain plume melts with depleted N-MORB type melts from the upper mantle or plume. EMII-like flavors in the old WGSC crust (A) are interpreted to originate from small-scale heterogeneities within the transition zone or upper mantle that are entrained into the northern part of the Galápagos plume. Seamount 63 lavas are interpreted to be low-degree melts derived directly from Northern Galápagos Domain plume material without significant dilution by melts from a depleted N-MORB type source. The presence of off-axis Seamount 63 with Northern Domain composition demonstrates that small amounts of plume mantle are able to flow beneath and to the far side (north) of the ridge axis.

Figure 1

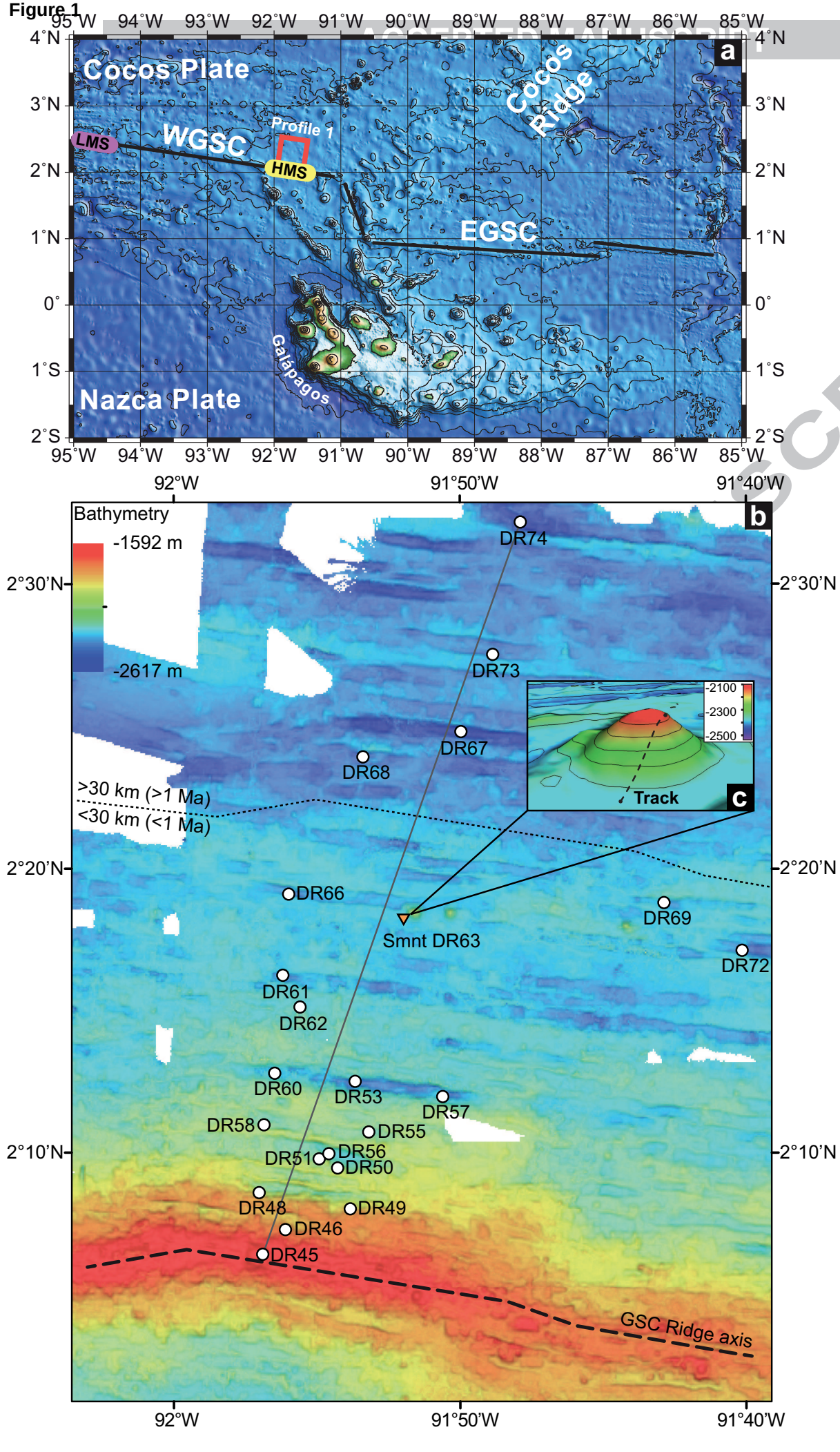

Figure 2

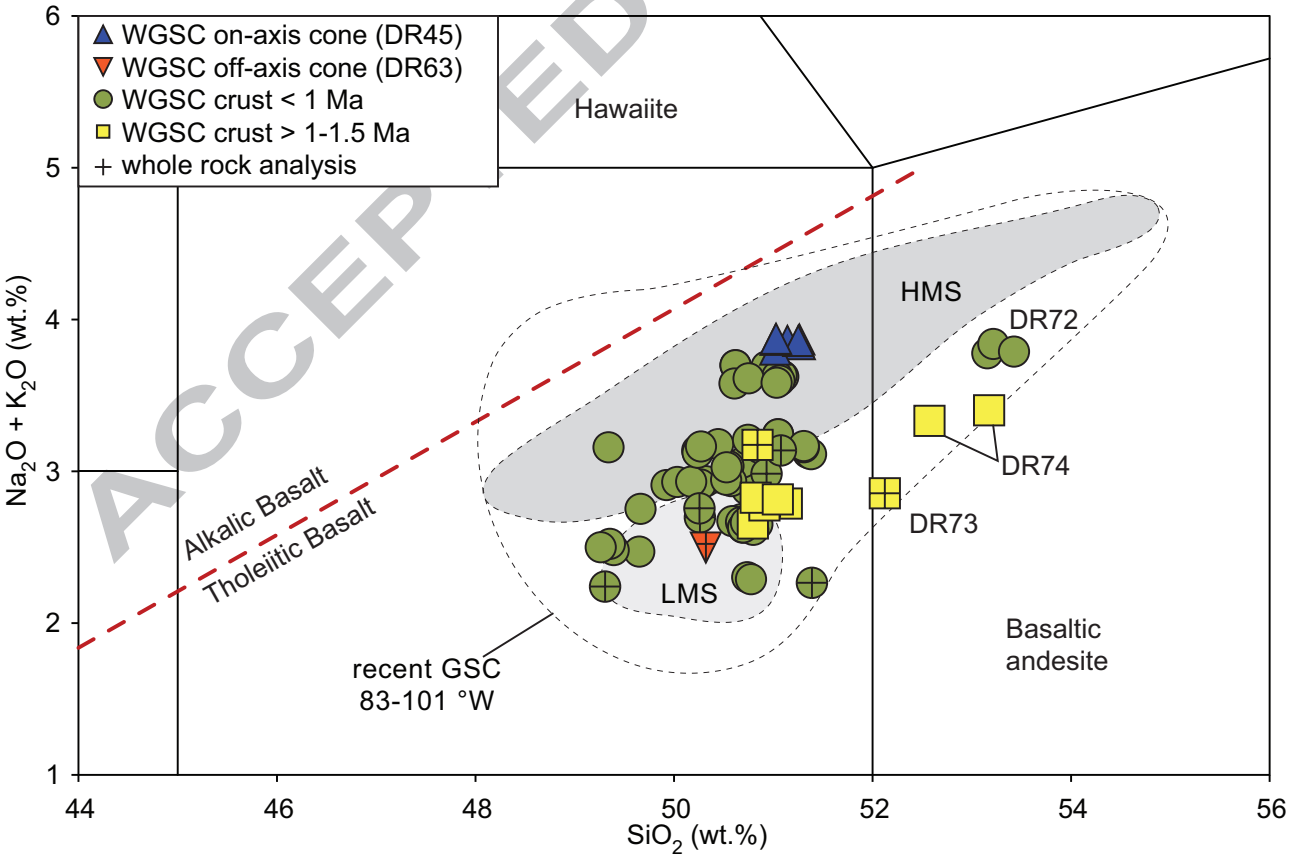

Figure 3

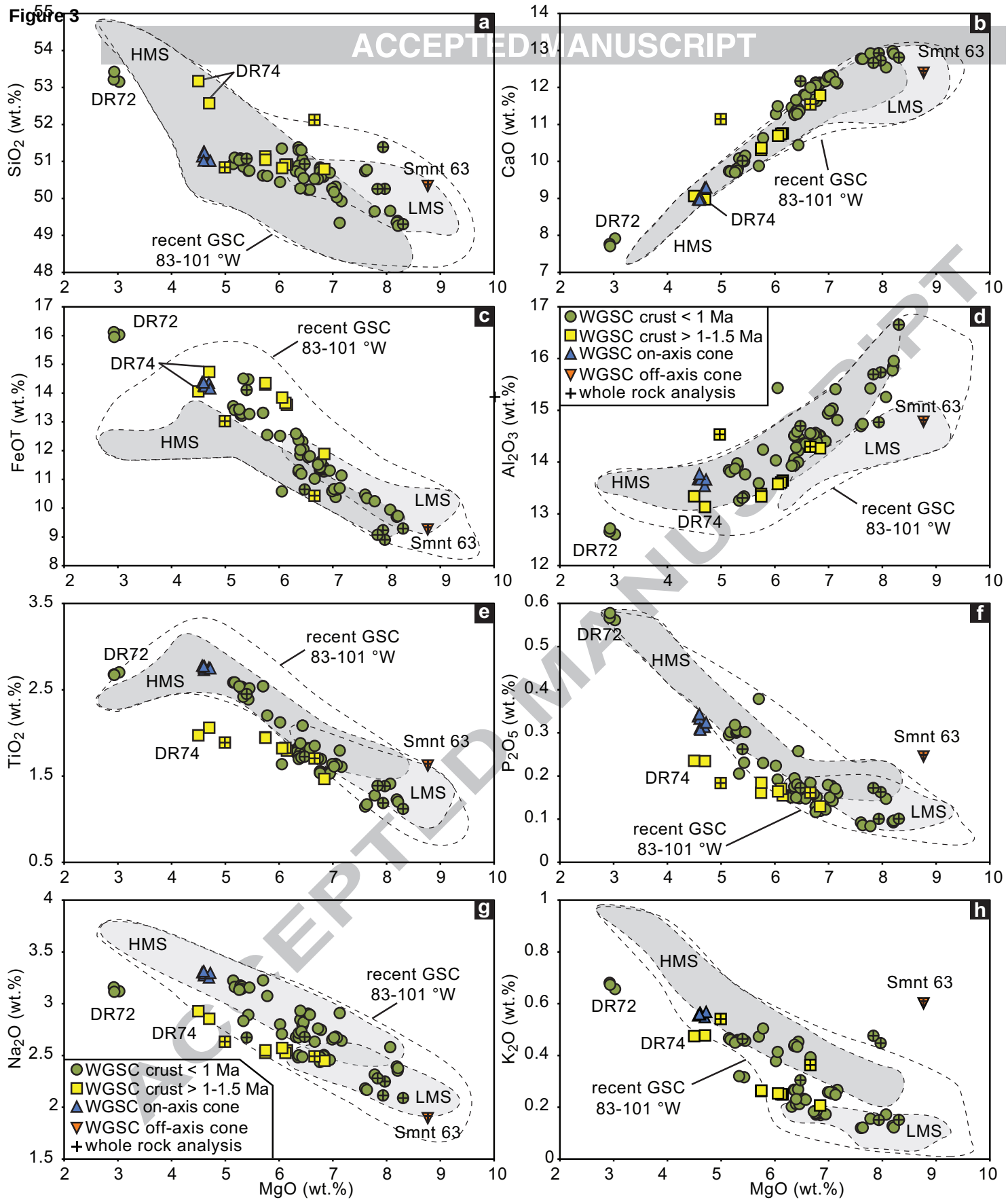

Figure 4

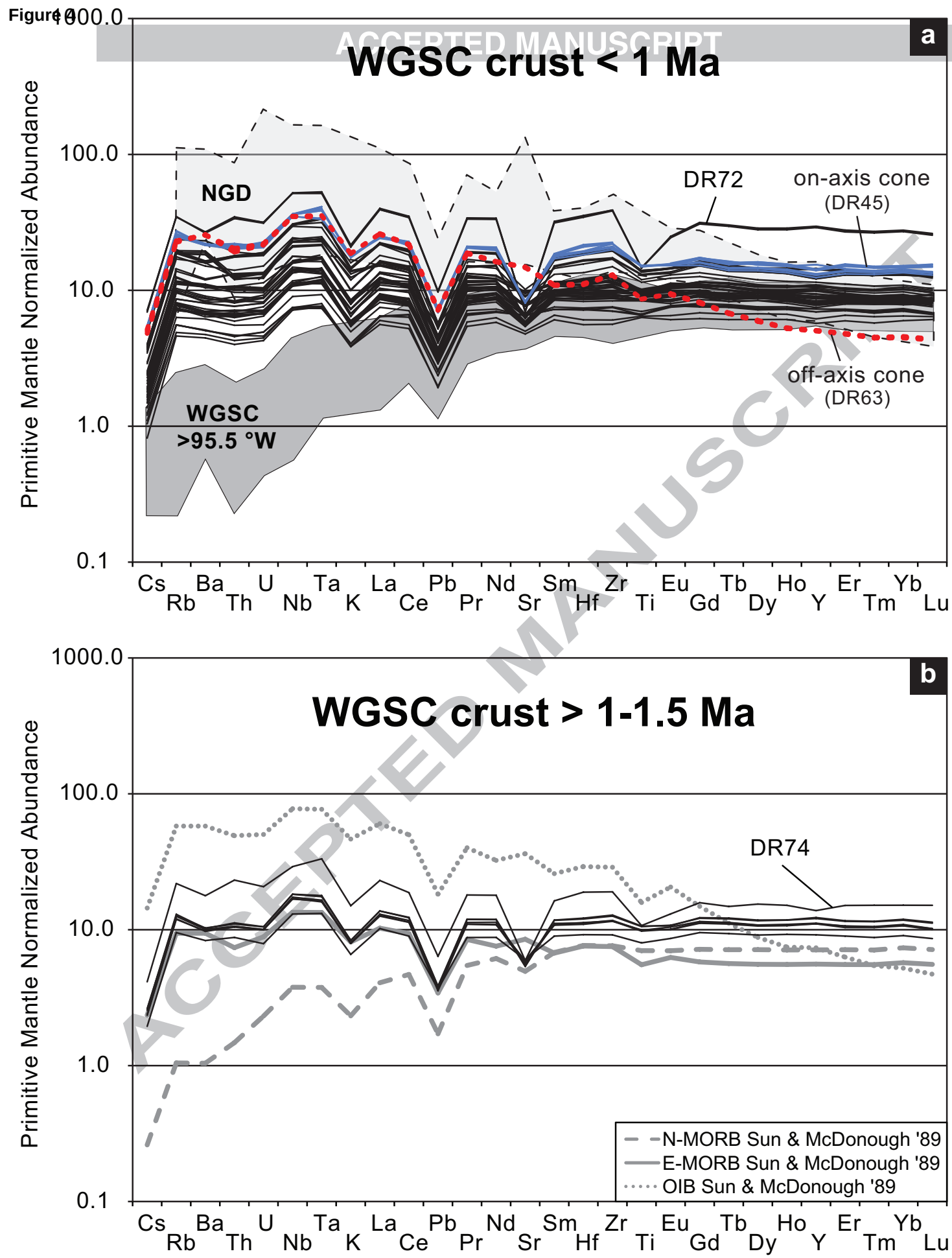

Figure 5

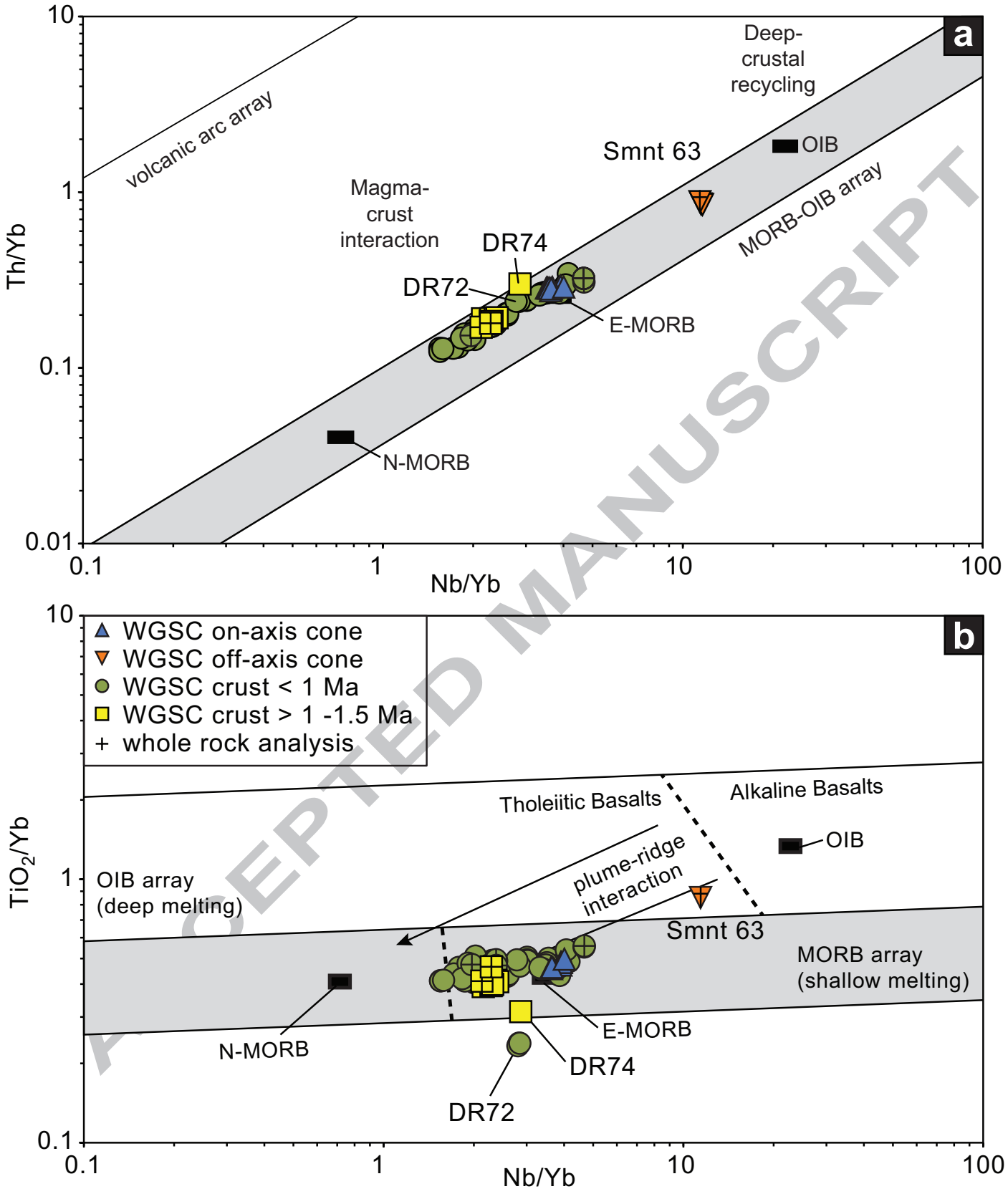

Figure 6

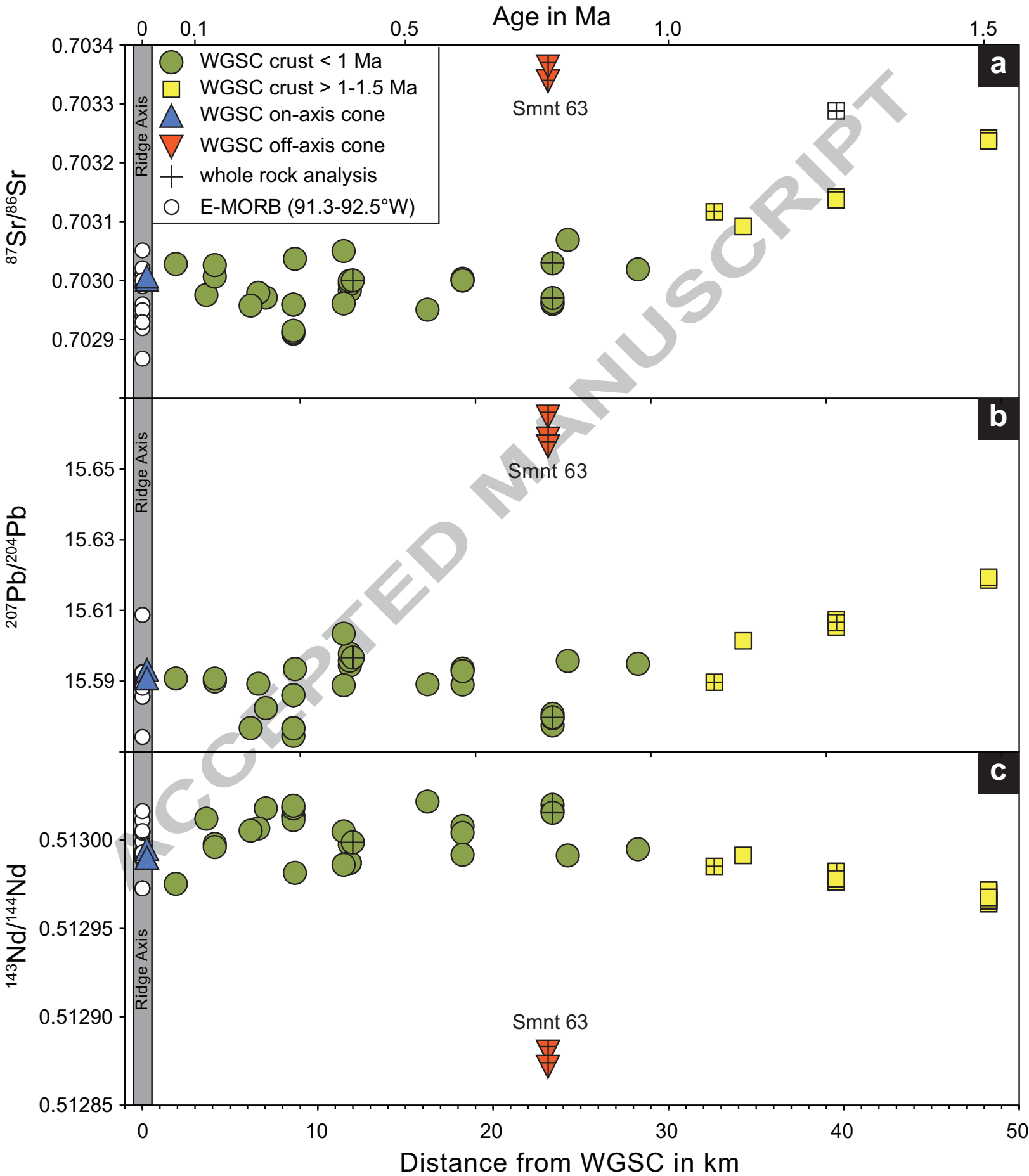

Figure 7

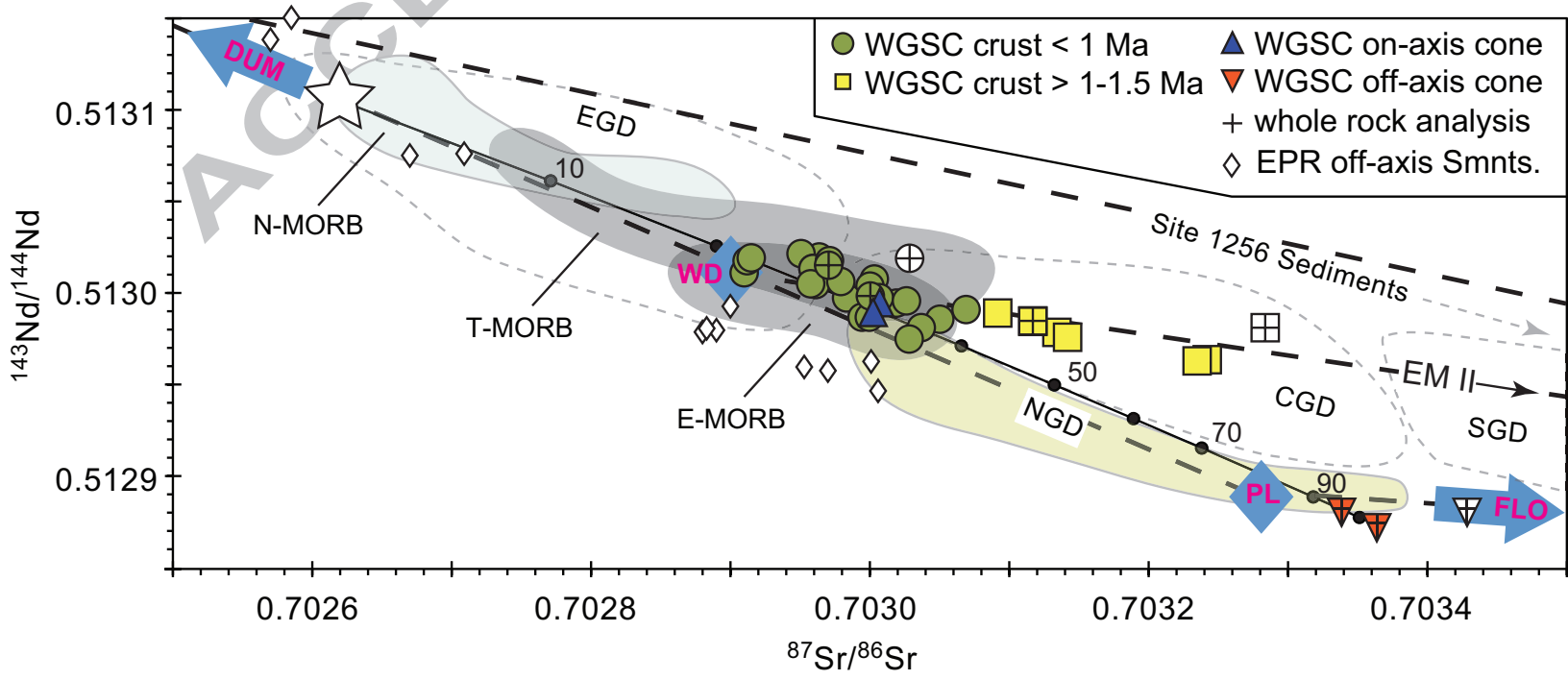

Figure 8

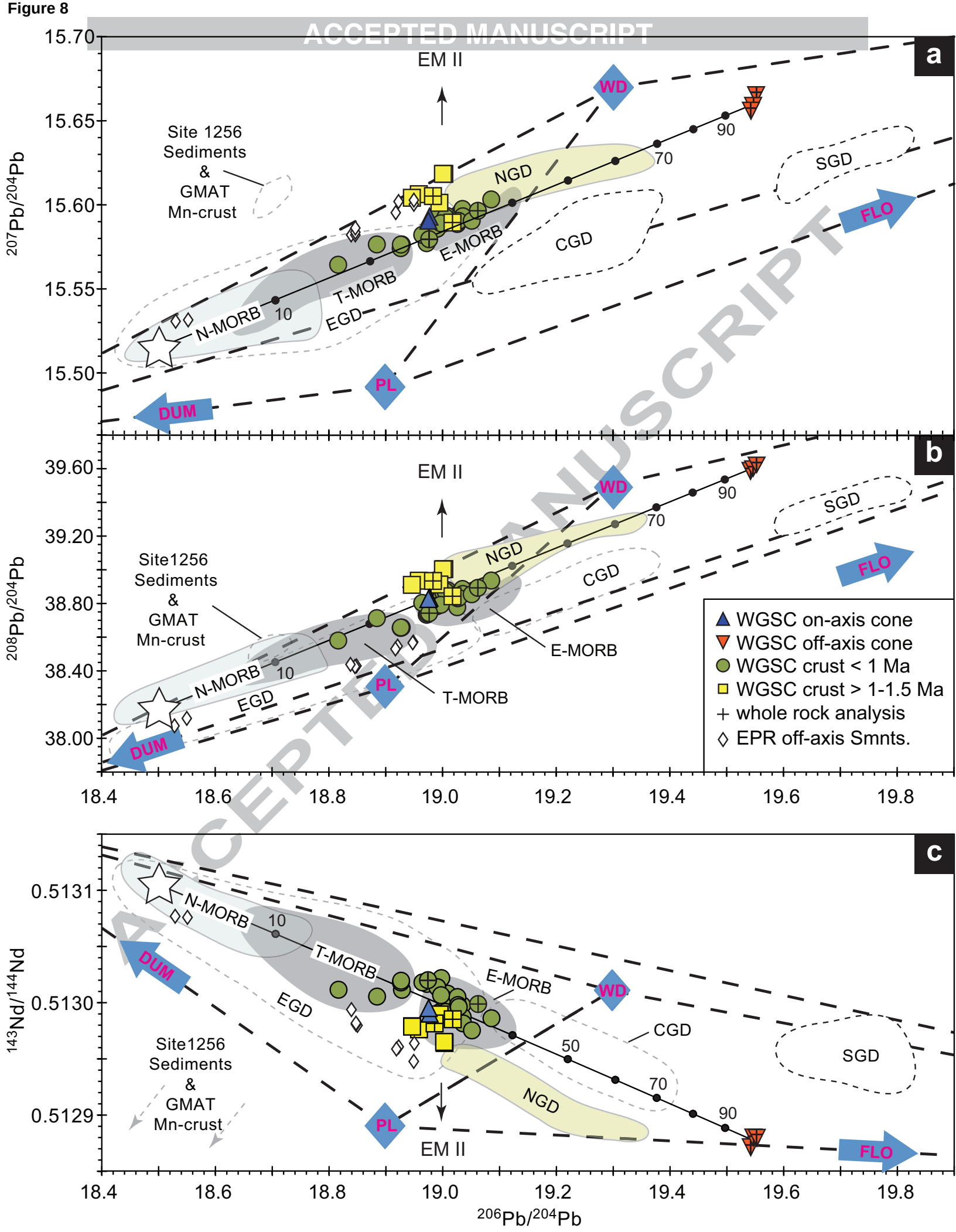

Figure 9

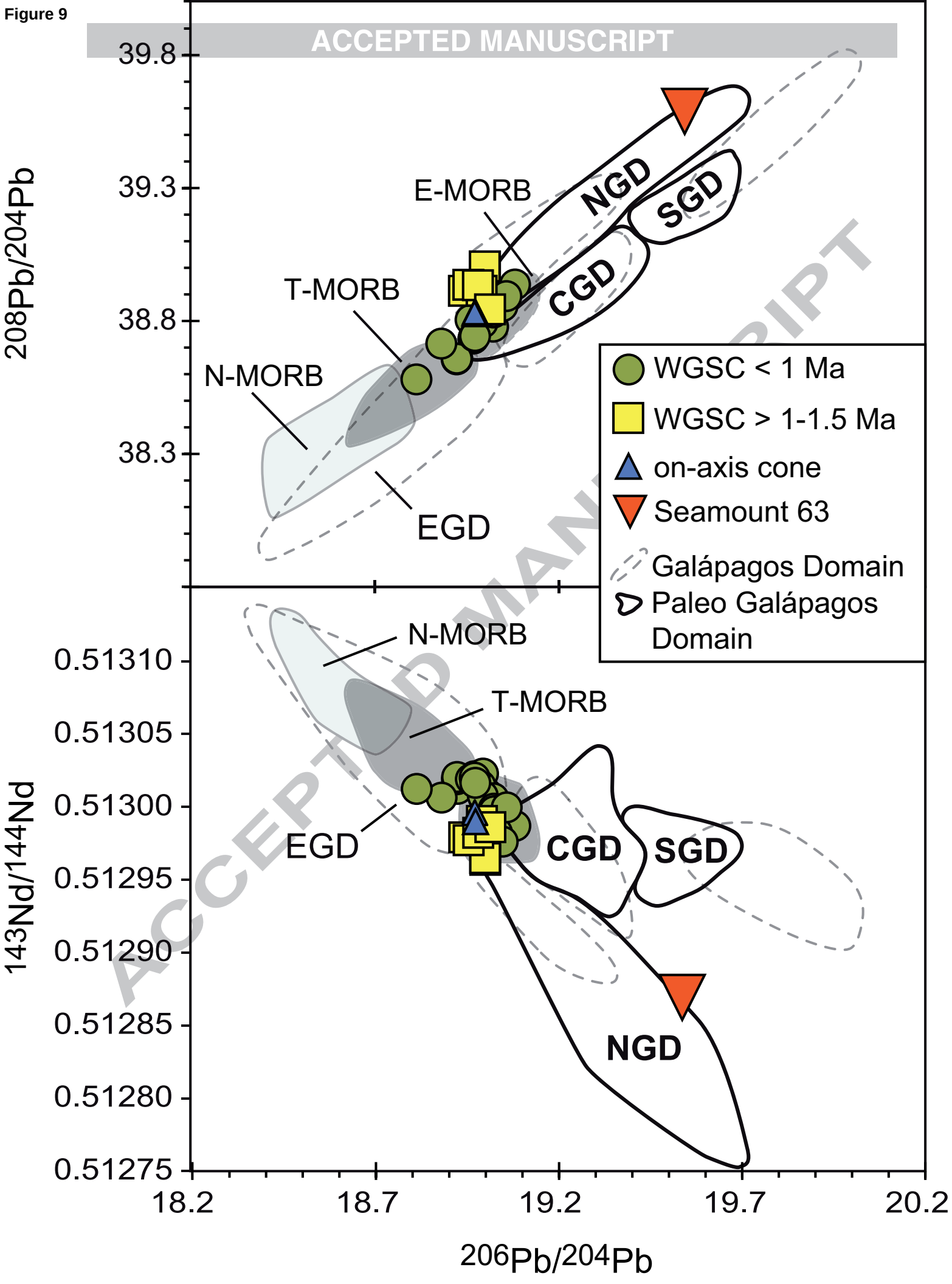

Figure 10